

SPECTROSCOPIC, ELECTROCHEMICAL, AND COMPUTATIONAL STUDIES ON AN
[FeFe]-HYDROGENASE ACTIVE SITE MIMIC WITH A TERTHIOPHENE BRIDGING
THE 2Fe2S CORE

by

Steven M. Sill

Copyright © Steven M. Sill 2014

A Thesis Submitted to the Faculty of the

DEPARTMENT OF CHEMISTRY AND BIOCHEMISTRY

In Partial Fulfillment of the Requirements

For the Degree of

MASTER OF SCIENCE
WITH A MAJOR IN CHEMISTRY

In the Graduate College

THE UNIVERSITY OF ARIZONA

2014

STATEMENT BY AUTHOR

This thesis has been submitted in partial fulfillment of requirements for an advanced degree at the University of Arizona and is deposited in the University Library to be made available to borrowers under rules of the Library.

Brief quotations from this thesis are allowable without special permission, provided that an accurate acknowledgment of the source is made. Requests for permission for extended quotation from or reproduction of this manuscript in whole or in part may be granted by the head of the major department or the Dean of the Graduate College when in his or her judgment the proposed use of the material is in the interests of scholarship. In all other instances, however, permission must be obtained from the copyright holder.

SIGNED: Steven M. Sill

APPROVAL BY THESIS DIRECTOR

This thesis has been approved on the date shown below:

Dennis L. Lichtenberger
Professor of Chemistry

February 17, 2014
Date

ACKNOWLEDGEMENTS

During the time I spent at the University of Arizona I was fortunate to interact and collaborate with many great individuals that provided guidance as well as a friendship that helped during those stressful times of my independent research towards my Master of Science degree. I would first and foremost like to thank my advisor, Prof. Dennis L. Lichtenberger. He provided me with the opportunity to achieve the role of an independent research scientist through his encouragement, guidance and support over the years in his research group. I would also especially like to thank Prof. Richard S. Glass for the time I was able to interact with him and his ever available guidance that was invaluable on the collaborative research project.

Additionally, I would like to thank all of the members of the Lichtenberger group, past and present, for their support as co-workers and amazing interactions as friends. I would especially like to thank Elliott Smith, Gabriel Hall, Susan Borowski, Takahiro Sakamoto, and Laura Stratton for their wonderful scientific discussions and contributions, for proofreading manuscripts and my thesis, and for being wonderful friends during my time in the Lichtenberger group.

Lastly, I would like to thank my family, who without them and their encouragement, guidance, and emotional support, none of this would have been possible. I can't thank my family and friends enough for everything they have provided.

Table of Contents

List of Figures.....	6
List of Schemes	8
List of Tables	9
ABSTRACT	10
Chapter 1 : INTRODUCTION.....	11
Hydrogenase	12
[FeFe]-hydrogenase active site mimics	15
Photocatalytic H ₂ production using [FeFe]-hydrogenase mimics	19
Chapter 2 : EXPERIMENTAL	25
Preparation of compounds	25
General comments.....	25
Preparation of 4,5-bis-(hydroxythiophene-2-yl-methyl)-[1,3]dithiole-2-thione, 10 ⁵¹	26
Preparation of [5-(thiophene-2-carbonyl)-2-thioxo-[1,3]dithiol-4-yl]thiophene-2-yl-methanone, 11 ⁵¹	27
Preparation of 4,5-bis(thiophene-2-carbonyl)[1,3]dithiole-2-one, 12 ⁵¹	27
Preparation of 4,6-di-thiophene-2-yl-thieno[3,4- <i>d</i>][1,3]dithiol-2-one, 13 ⁵¹	27
Preparation of (2,5-bis-(2',2''-thiophen-2-yl)-thiophene- μ -3,4-dithiolato)diiron hexacarbonyl, 1 (terthiophene-cat)	28
Computational methodology	28
Electrochemistry	29
Single-crystal X-ray diffraction.....	29
Chapter 3 : SYNTHESIS OF (2,5-BIS-(2',2''-THIOPHEN-2-YL)-THIOPHENE- μ -3,4-DITHIOLATO)DIIRON HEXACARBONYL.....	31
Introduction	31
Results and Discussion	33
(2,5-bis-(2',2''-thiophen-2-yl)-thiophene- μ -3,4-dithiolato)diiron hexacarbonyl.	33
Conclusion	40
Chapter 4 : CHARACTERIZATION OF (2,5-BIS-(2',2''-THIOPHEN-2-YL)-THIOPHENE- μ -3,4-DITHIOLATO)DIIRON HEXACARBONYL	41
Introduction	41
Nuclear Magnetic Spectroscopy	41
Infrared Spectroscopy: CO stretching frequency	48
X-Ray Crystal Structure	50

Ultraviolet-visible Spectroscopy	54
Conclusions	57
Chapter 5 : ELECTROCHEMISTRY AND COMPUTATIONAL VALIDATIONS FOR (2,5-BIS-(2',2''-THIOPHEN-2-YL)-THIOPHENE- μ -3,4-DITHIOLATO)DIIRON HEXACARBONYL	58
Introduction	58
Results and Discussion	62
Electrochemical Investigations	62
Catalysis	67
Comparison of Computations to Experimental Observed Values	70
Conclusions	74
Chapter 6 : CONCLUSIONS AND FUTURE DIRECTIONS	77
Effect of the 2,5-bis-(2',2''-thiophen-2-yl)-thiophene- μ -3,4-dithiolato ligand	77
Future Directions	79
REFERENCES:	81

List of Figures

Figure 1.1. Active site of the [FeFe]-hydrogenase enzyme, with the central bridgehead group (X) in the dithiolate linker being represented as either CH ₂ , NH, or O.	14
Figure 1.2. Crystal structure of the [FeFe]-hydrogenase active site with PDT overlaid (solid black lines).....	16
Figure 1.3. The molecules of interest that are discussed in this work, with 1 being the focus....	17
Figure 1.4. Two-component system [FeFe]-hydrogenase mimics 4-7 used for photocatalytic H ₂ production.	21
Figure 1.5. Three-component system [FeFe]-hydrogenase mimics 8 and 9 used for photocatalytic H ₂ production.	22
Figure 3.1. Infrared spectroscopy of the carbonyl stretching frequency region (wavenumbers, cm ⁻¹) collected to track the reaction progress of 13 with Fe ₂ (CO) ₉ in toluene.....	37
Figure 4.1. ¹ H NMR spectrum of 1 in CDCl ₃ . Residual benzene solvent absorption is indicated with the asterisk.	43
Figure 4.2. ¹³ C NMR of 1 in CDCl ₃	44
Figure 4.3. Heteronuclear Single Quantum Correlation (HSQC) NMR spectroscopy of 1 in CDCl ₃ . ¹ H NMR spectrum is displayed on the horizontal axis and the ¹³ C NMR spectrum is displayed on the vertical axis.	45
Figure 4.4. Heteronuclear Multiple Bond Correlation (HSQC) NMR spectroscopy of 1 in CDCl ₃ . ¹ H NMR spectrum is displayed on the horizontal axis and the ¹³ C NMR spectrum is displayed on the vertical axis. The boxed peaks are artifact ¹ J _{CH} couplings.	46
Figure 4.5. Comparison of the experimental IR spectra in the carbonyl stretching frequency region for 1 , 2 , and 3 . All spectra were collected in hexanes using an air-free IR cell.	49
Figure 4.6. Thermal ellipsoid plot of 1 obtained by X-ray crystal diffraction with thermal ellipsoids at the 50% probability level.....	51
Figure 4.7. UV-visible absorption spectra comparison of 1 (solid line) and 3 (dashed line) in the listed solvents in the inset.	55
Figure 5.1. Catalytic mechanism for 3 in acetonitrile with the calculated (blue) and experimental (black) values for the reduction potentials.....	61
Figure 5.2. Cyclic voltammogram of 1 in dichloromethane with 0.2 M tetra- <i>n</i> -butylammonium hexafluorophosphate on a 0.3 cm diameter glassy carbon working electrode at a scan rate of 0.100 V/s under an argon atmosphere. The black arrow indicates the direction of the initial scan. The dashed lines indicate the half-wave potential for ca. 1 mM 1 (blue), 1 mM 2 (red), and 0.5 mM 3 (green).	64
Figure 5.3. Cyclic voltammograms of 1 mM 1 (left) and 2 (right) collected in CH ₂ Cl ₂ with 0.2 M tetra- <i>n</i> -butylammonium hexafluorophosphate on a 0.3 cm diameter glassy carbon working electrode. Scan rates are listed for each complex.	65
Figure 5.4. Comparison of the HOMO (bottom) and LUMO (top) plots of 1 (left), 2 (middle) and 3 (right).	66
Figure 5.5. Cyclic voltammogram of ca. 1 mM 1 in the presence of various acetic acid concentrations with 0.2 M tetra- <i>n</i> -butylammonium hexafluorophosphate in CH ₂ Cl ₂ on a glassy carbon working electrode at a 0.10 V/s scan rate under an Ar atmosphere. The black arrow indicates the direction of the initial scan.....	68

- Figure 5.6.** Voltammogram of ca. 1 mM **1** (blue) and **2** (red), and ca. 0.5 mM **3** (green) in the presence of 50 mM acetic acid at 0.10 V/s with 0.2 M tetra-*n*-butylammonium hexafluorophosphate in CH₂Cl₂. The black arrow indicates the initial scan direction. 69
- Figure 5.7.** Experimental (black) and calculated (blue) carbonyl stretching frequencies of **1**. The experimental frequencies were collected in hexanes using an air-free IR cell. 72
- Figure 5.8.** Proposed catalytic mechanism for **1** for the reduction of protons to H₂. 76

List of Schemes

Scheme 3.1. <i>i.</i> Reaction of $\text{Fe}_2(\text{CO})_9$ with 1,2-benzenedithiol. <i>ii.</i> Reaction of $\text{Fe}_3(\text{CO})_{12}$ with 1,2-benzenedithiol. <i>iii.</i> Reaction $\text{Fe}_2\text{S}_2(\text{CO})_6$ with superhydride and trifluoroacetic acid to produce the $\text{Fe}_2(\text{SH})_2(\text{CO})_6$ intermediate, and the following reaction with 1,4-naphthoquinone and piperidine. <i>iv.</i> Reaction with 1,4-benzoquinone and $\text{Fe}_2\text{S}_2(\text{CO})_6$ in benzene using irradiation.....	32
Scheme 3.2. Synthetic route of lithium 3,4-thiophenedithiolate (middle) followed by protonation to the 3,4-thiophenedithiol (right).....	34
Scheme 3.3. Proposed synthesis for preparing 14 (top) which failed, and the major products obtained (bottom) from the reaction.	35
Scheme 3.4. <i>Top:</i> Synthesis of 11 from vinylene trithiocarbonate and two consecutive additions of lithium diisopropylamide (LDA) and 2-thiophenecarboxaldehyde, followed by oxidation of the intermediate product with MnO_2 . <i>Middle:</i> Conversion of the trithiocarbonate to the dithiocarbonate, 12 . <i>Bottom:</i> Ring closure reaction using P_4S_{10} and NaHCO_3 in 1,4-dioxane. ...	38
Scheme 3.5. Synthesis of complex 3	39

List of Tables

Table 4.1. 1D and 2D NMR assignment of 1 in CDCl ₃	47
Table 4.2. X-ray crystallographic parameters for 1	52
Table 4.3. Selected bond lengths and angles obtained from crystallographic data of 1 , 2 , and 3	53
Table 4.4. Absorption band of 1 and 3 in the visible region in four solvents with varying dielectric constants and the corresponding ϵ value.	56
Table 5.1. Comparison of the DFT geometry optimized structure to the X-ray crystallographic data for 1	71

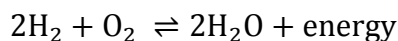
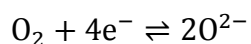
ABSTRACT

As a means of reducing the dependence on fossil fuels, generation of hydrogen (H_2) has been proposed as a route for storing energy in a chemical bond. To access this energy, H_2 can be combusted with oxygen or used in a fuel to release the energy stored in the chemical bond, while generating water as the byproduct. To generate the hydrogen necessary to fuel a hydrogen economy, an energy efficient and stable catalyst needs to be designed. The work presented in this thesis describes the investigation of a catalytic mimic inspired by the [FeFe]-hydrogenase enzyme. The design of this and similar mimics have been pursued as the active site of the enzyme is composed of readily available and abundant elements, and has a turnover rate of 6000-9000 molecules of H_2 s^{-1} . The catalyst in this work was studied via cyclic voltammetry and density functional theory calculations to determine the catalytic activity as well as a mechanism for H_2 production of the complex.

The complex 2,5-bis-(2',2''-thiophen-2-yl)-thiophene- μ -3,4-dithiolato)diiron hexacarbonyl, **1**, was prepared and found to catalyze the production of molecular hydrogen in CH_2Cl_2 , however the overpotential for catalysis was not determined as the standard potential of acetic acid in CH_2Cl_2 is not known. Comparison of the catalytic potentials of terthiophene-cat to μ -(1,2-benzenedithiolato)diiron hexacarbonyl, **2**, and μ -(3,4-thiophenedithiolato)diiron hexacarbonyl, **3**, in CH_2Cl_2 showed that **1** had a less negative potential (0.14 V and 0.16 V, respectively) for the catalytic reduction of protons to H_2 . Electrochemical investigations combined with density functional theory (DFT) indicated that **1** has an ECEC mechanism for the reduction of protons, where E is an electrochemical step and C is a chemical process. The proposed mechanism for **1** is similar to that of **2** and **3**, with **1** catalyzing the production of H_2 using acetic acid at a less negative potential than **2** and **3**.

Chapter 1 : INTRODUCTION

There is a pressing need to decrease the energy dependence on fossil fuels by shifting to more sustainable and renewable source of energy. Fossil fuels are a limited resource that have been harvested in the inexpensive, and readily accessible locations, and new locations that are found subsequently have a higher cost of operation to collect the fossil fuels.¹ In conjunction with these costs, it's projected that the global energy consumption will increase by 56% from 524×10^{12} British thermal units (Btu) in 2010 to 820×10^{12} Btu in 2040, with 80% of the total energy usage being supplied by fossil fuels. Consequently, this will cause a projected increase of the CO₂ emissions by 46% in that same time span. The need for an alternative fuel source is apparent due to both the rising cost and large consumption of fossil fuels to supply the energy demand. At present, there are methods in place for taking advantage of renewable energy sources such as solar, wind, geothermal, hydroelectric and wave turbines that generate electricity. However, though these sources generate usable energy, if it isn't used immediately, then that energy is lost if isn't stored. A method for storing this energy so that it can be used at a later time is required, and a way of doing this is by storing that energy in a chemical bond, specifically molecular hydrogen.^{2,3} To access the stored energy, the hydrogen can be combusted with oxygen to generate thermal energy and water as a byproduct. Alternatively, it can be used as fuel in a proton exchange membrane fuel cell (PEMFC) where hydrogen is oxidized at a platinum electrode to protons, and oxygen is reduced to water at the cathode, with electricity being generated in the process.⁴



Methods are in place for producing molecular hydrogen, such as steam reformation⁵ and electrolysis of water.⁶ However, steam reformation involves the use of fossil fuels, and high temperatures to produce hydrogen. For the electrolysis of water, platinum is currently the most efficient catalyst, but it's an expensive and relatively low abundant metal, preventing large scale operations from being used to produce molecular hydrogen. To efficiently generate the molecular hydrogen needed to provide power for the future, a cheaper and more readily abundant catalyst is required that can be used for large scale production. A series of enzyme catalysts that meet these requirements already exist in Nature, known as the hydrogenase family, efficiently reduce protons to hydrogen and are used as a foundation for designing functional mimics for H₂ production.⁷⁻⁹

Hydrogenase

The hydrogenase enzymes that are responsible for the reversible reduction of protons to hydrogen are found in bacteria known as *Desulfovibrio desulfuricans* and *Clostridium pasteurianum* and was first discovered by Stephenson and Stickland.¹⁰ Since the initial discovery, only four unique types of hydrogenase enzymes have been identified, and they are referred to by the core of their metal/metal bond framework at the active site. These four enzymes are the [NiFe], [NiFeSe], [FeFe], and [Fe]-only.¹¹⁻¹⁶ All of these enzymes function to reversibly catalyze the reduction of protons to hydrogen, and of these four, the [FeFe]-hydrogenase enzyme has been found to be the most efficient at the reduction of protons with a rate of 6000-9000 molecules of H₂ s⁻¹ for each active site.⁹ Unfortunately, all of the hydrogenase enzymes are sensitive to both light and air, and it is therefore impractical to try to make a large scale implementation of the hydrogenase enzyme,³ but functional mimics are being investigated using information provided by X-ray crystallographic data{ 1443 Nicolet 2000; } that showed the [FeFe]-hydrogenase active site has two irons connected by a dithiolato bridge.^{2,17,18} This bonding form is known as a butterfly

structure with the 2Fe2S core, shown in Figure 1.1. Debate continues as to the true structure of the dithiolato bridge, as the resolution of the crystal structure is not high enough to elucidate if the central bridgehead group, X, is either a CH₂, NH, or O.¹⁹ It was originally speculated to be CH₂, but recent work suggests that it is an NH group.²⁰ The proximal Fe atom of the active site is bound to a cysteine and [4Fe4S] cubane through a sulfur bound at the apical position on one of the two iron atoms and this is hypothesized to be the electron relay to the active site for the proton reduction. The remaining basal ligands on both iron atoms are CO and CN⁻ with a bridging CO between the two iron atoms. Carbon monoxide and cyanide ions are toxic to living organisms, which makes their presence as ligands at the active site of the enzyme unique. A vacant site is found on the distal iron atom, where it is suggested that the H-H bond formation occurs.

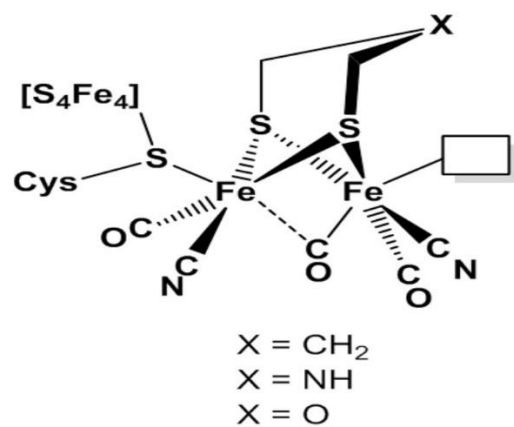


Figure 1.1. Active site of the [FeFe]-hydrogenase enzyme, with the central bridgehead group (X) in the dithiolate linker being represented as either CH₂, NH, or O.

[FeFe]-hydrogenase active site mimics

After crystallographic determination of the active site of the [FeFe]-hydrogenase enzyme,¹⁹ focus returned to previously reported compounds that contained a similar structural architecture in the core.²¹ Darensbourg et al. compared the crystal structure of the active site of the enzyme to the previously known complex μ -(propanedithiolato)diiron hexacarbonyl (PDT) complex, and found that the two were structurally similar, as shown in Figure 1.2.²² Although structurally similar, when tested for its electrocatalytic ability to produce H_2 using acetic acid as the proton source, it was found that PDT catalytically reduced protons at -2.35 V vs Fc^+/Fc , which is a -0.89 V overpotential and not ideal for use in large scale production.^{23,24} Despite the drawbacks, the successful catalytic production of H_2 inspired others to look at ways to modify the hydrogenase mimic to produce molecular hydrogen more efficiently.¹⁷ One such modification was replacing the propanedithiolate bridgehead with a benzenedithiolate, a ligand similar to the ene-dithiolates that are believed to provide stabilization to Mo/W enzymes at varying oxidation states.²⁵⁻²⁹ In the μ -(1,2-benzenedithiolato)diiron hexacarbonyl, **2**, complex, it was found that the molecular structure of this mimic undergoes a geometric rearrangement upon either oxidation or reduction to a structure with a bridging carbonyl between the Fe centers, similar to the active site [FeFe]-hydrogenase geometry.^{2,30} Electrochemically, **2** was found to have a reversible and two-electron reduction peak, due to a potential inverse process, at a lower potential compared to PDT in acetonitrile.^{30,31}

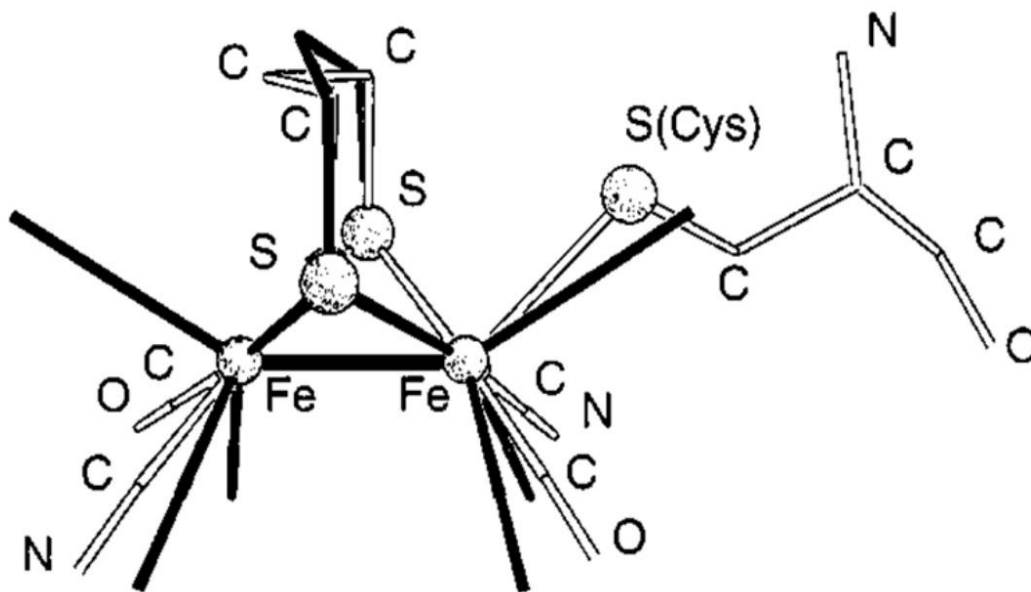


Figure 1.2. Crystal structure of the [FeFe]-hydrogenase active site with PDT overlaid (solid black lines).

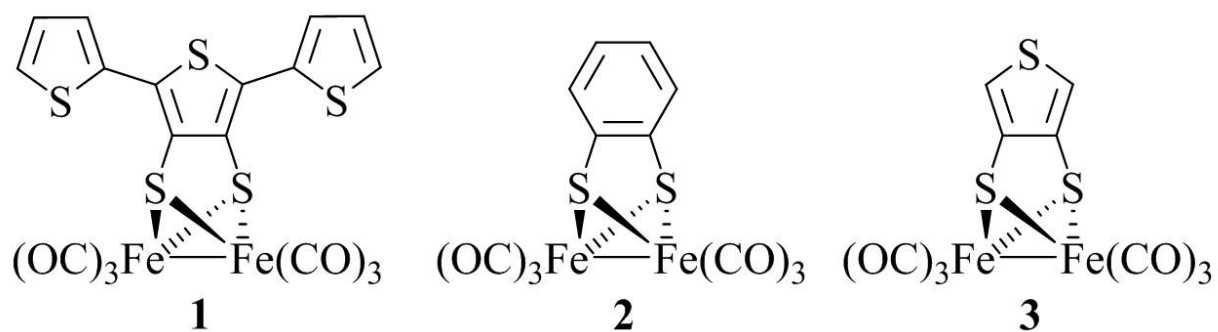


Figure 1.3. The molecules of interest that are discussed in this work, with **1** being the focus.

A potential inverted process is observed when the thermodynamic potential for the second reduction is more positive than the first, indicating that the thermodynamic potential for second reduction is more favorable than the first. It was also shown that **2** was capable of generating molecular hydrogen from acetic acid at a lower overpotential than PDT, -0.49 V^{30} vs -0.89 V^{23}

After the success of **2**, μ -(3,4-thiophenedithiolato)diiron hexacarbonyl, **3**, was generated by replacing the 1,2-benzenedithiolate reactant with the isoelectronic 3,4-thiophenedithiolate in the synthetic reaction as a proof-of-concept catalyst to determine if molecular hydrogen production would be maintained.³² In the work with **3**, similarities were observed when compared to **2**, such as the first reduction occurring at the same potential, -1.33 V , as a reversible, potentially inverted two electron reduction. A comparable overpotential of -0.44 V was observed with **3** using a glassy carbon electrode (GCE) and acetic acid for the production of molecular hydrogen.³² Density functional theory (DFT) calculations indicated that both **2** and **3** have a similar mechanistic pathway for production of molecular hydrogen, and that upon reduction to the dianion, both catalysts have an Fe-S bond that elongates and a carbonyl rotates into a bridging position between the iron centers.^{30,32} This molecular rearrangement after the first reduction to the anion allows the second reduction to occur at a potential lower than the first, and the catalysts are further reduced to the dianion. In the rotated geometry, an open site is available for protonation between the Fe centers, and the calculated pK_a 's indicate that the dianion structure is basic enough for protonation by acetic acid to occur. However, no catalysis was seen at the first reduction for either catalyst after the initial protonation, therefore meaning a third electron is required at a more negative potential than the initial two electron reduction, resulting in a catalytic peak for **2** at -1.95 V^{30} and **3** at -1.91 V^{32} vs Fc^+/Fc . As such, these two catalysts were observed to produce molecular

hydrogen through an (E)ECEC mechanism with the first electron, (E), being required only once to generate the active catalyst from the precatalyst.

Photocatalytic H₂ production using [FeFe]-hydrogenase mimics

An alternative method for production of molecular hydrogen is through the capture of sunlight with a photosensitive complex, using Nature's photosynthesis process as a guide. In this process, there are three fundamental steps that must occur. The first step is the capture of the energy from a photon at a photosensitizer (PS), such as chlorophyll. The second is the transfer of the photo-excited electron to create the spatially separated electron/hole pair. The third step is catalysis, where the generated hole is captured by the oxygen-evolving complex to oxidize water to oxygen, and the electrons are captured at photosystem I to reduce protons to H₂.³³ However, with the photosensitive mimics, there is no photosystem I present to fill the holes generated, therefore electron donors are necessary, such as triethylamine or ascorbic acid. Attempts have been made by groups to generate artificial photosynthetic complexes that incorporate these concepts by having a PS connected to a [FeFe]-hydrogenase functional mimic (two-component system) or mixed with the [FeFe]-hydrogenase mimic in solution (three-component system).³⁴⁻³⁷ For the two-component systems, the PS can be bound to one of two places, either at the bridging dithiolate linker of the 2Fe2S core, or directly bound to one of the Fe atoms. Sun's group was the first to generate and explore the two-component model photosynthetic catalysts, **4-6**, by linking a ruthenium (II) bipyridine PS to the dithiolate linker in **4** and **5**, and directly linking the PS to one of the Fe atoms in **6**,³⁸⁻⁴⁰ while Song's group investigated a zinc-porphyrin complex bound to the dithiolate linker, **7**.⁴¹

Although these complexes were not capable of generating molecular hydrogen photocatalytically, it was determined that the selection of the photosensitizer ligand is important,

due to a negative shift of the first reduction potential of these model complexes compared to the respective unmodified [FeFe]-hydrogenase mimic.^{39,40} When the complexes were studied via time-resolved absorption spectroscopy, the quenching of the excited states were attributed to loss of thermal energy instead of electron transfer, and photo-degradation of the complexes **4-6**.³⁸⁻⁴⁰ The negative shift of the initial reduction may be a reason for the poor electron transfer that is observed between the PS and the 2Fe2S core, as it was determined to not be a favorable transition from the time-resolved absorption spectroscopy. After complexes **4-6** were reported, similar photocatalytic mimics were designed using zinc-porphyrin^{37,42-44} and rhenium(I) photosensitizers⁴⁵ with little to no modification to the aromatic linker between the photosensitizer and the [FeFe]-hydrogenase mimic. These reported complexes were able to generate H₂ photocatalytically, but with very low turnover numbers (TON) of 0.08 to 1.96. An improvement was observed in H₂ generation using the smaller [FeFe]-hydrogenase mimics, **8**⁴⁶ and **9**,⁴⁷ with an iridium or a ruthenium photosensitizer mixed with the photocatalyst in a three-component system. In these systems the PS was reduced by an electron donor in solution, either triethylamine or ascorbic acid, after photo-excitation to prevent the electron-hole recombination event from occurring. The reduced form of the respective photosensitizer was capable of transferring an electron to **8** and **9**, which was an improvement compared to **4-6** which were unable to transfer an electron based on the emission spectroscopy data.³⁸⁻⁴⁰ A large improvement in the turnover numbers for H₂ production was observed with **8** (466 TON) and **9** (200 TON) versus the previously reported 0.08 to 1.96 TON for the two-component systems.³⁴ However, for the H₂ generation to occur using complexes **8** and **9**, the PS in both experiments had to be reduced by the electron donor following photoexcitation before transfer of an electron to the catalyst was observed.^{46,47} This is one problematic issue for the three-component system due to the PS needing to be reduced first before an electron transfer will occur,

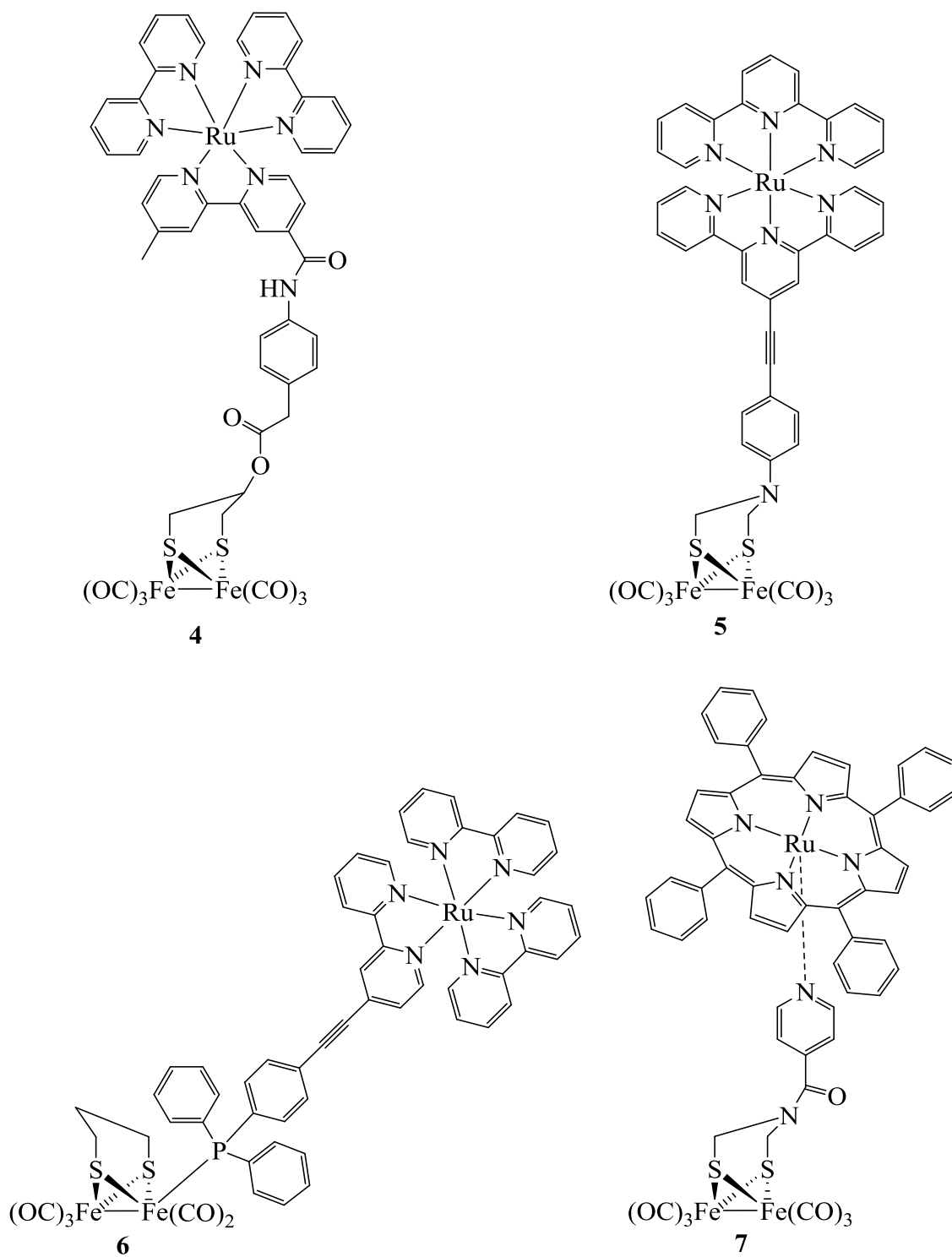


Figure 1.4. Two-component system [FeFe]-hydrogenase mimics **4-7** used for photocatalytic H₂ production.

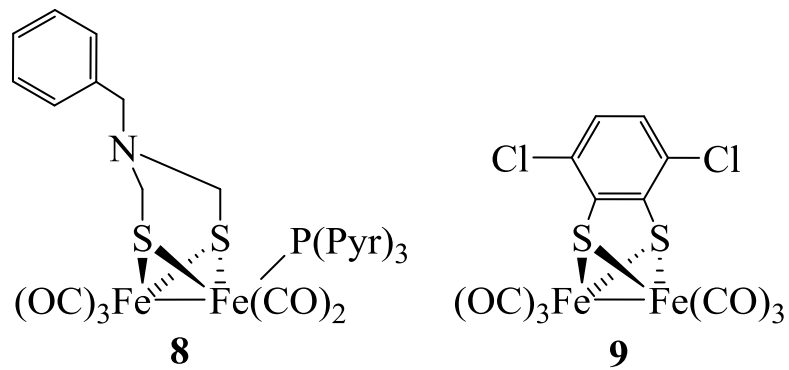


Figure 1.5. Three-component system [FeFe]-hydrogenase mimics **8** and **9** used for photocatalytic H_2 production.

followed by the second requirement of the reduced PS having a favorable interaction with the catalyst in solution. Higher concentrations of the electron donor and PS relative to the catalyst should improve the number of collisions in solution, improving the chances of an electron transfer. Another shortcoming of these systems was the degradation observed of the iridium PS⁴⁶ and the photocatalyst **9**.⁴⁷ Although an increase in the TON of H₂ production was observed with **8** and **9**, the stability of the photocatalytic complexes during the catalytic cycle still need to be improved to increase the photocatalysts' lifetimes. The photocatalyst mimics have primarily been studied in non-aqueous solvents due to poor solubility in water, and have shown improved turnover numbers since the first artificial photosynthetic complexes were introduced. Unfortunately, these mimics are still plagued with short lifetimes and decompose to inactive materials when exposed to prolonged irradiation (1 to 10 hours).^{34,38} Recently, a three-component system using a CdTe quantum dot, a water soluble [FeFe]-hydrogenase mimic catalyst and ascorbic acid as both the proton and electron donor, was reported with having a TON of 505, the highest presently reported.⁴⁸ Alternatively, rather than using a three-component system with a quantum dot absorbing a photon, a two-component system incorporating an oligothiophene can be used as a photosensitizer ligand for generation of electron-hole pairs.⁴⁹ These are a class of compounds that are known to have tunable absorption band properties upon modifying the conjugation,⁵⁰ and oligothiophenes are presently being used in solar cell applications. The work presented here focuses on replacing the monothiophene in **3** with a terthiophene system to generate (2,5-bis-(2',2''-thiophen-2-yl)-3,4-dithiolthiophene)diiron hexacarbonyl, **1**, while trying to maintain the catalytic ability for H₂ production. Additionally, **1** may be used as a proof-of-concept [FeFe]-hydrogenase mimic for photocatalytic H₂ production with the conjugated terthiophene acting as a photosensitizer which is directly connected to the bridging sulfurs of the 2Fe2S core rather than

through a long linker. This structural design may improve the quenching of the photoexcited state through a more favorable electron transition from the photoexcited PS to the 2Fe2S core.

Chapter 2 : EXPERIMENTAL

Preparation of compounds

General comments

All of the reactions in this thesis were performed under inert gas, nitrogen or argon, using Schlenk line techniques with an oxygen scrubber between the inert gas tank and the Schlenk line. All chemicals were used as received unless otherwise stated. Diiron nonacarbonyl, *n*-butyllithium (2.5 M and 1.6 M in hexanes), vinylene trithiocarbonate, 2-thiophene carboxaldehyde, phosphorus pentasulfide, diisopropyl amine, and charcoal were purchased from Sigma Aldrich. Sodium bicarbonate and 1,4-dioxane were purchased from EMD Chemicals. Calcium hydride was purchased from Alfa Aesar. Diisopropylamine and 1,4-dioxane were dried over CaH₂. Tetrahydrofuran (THF) was purchased from EMD Chemicals and was either dispensed using an MBraun Solvent Purification System (EMD OMNI-Solv unstabilized) or distilled prior to use. All other solvents were used as received for column chromatography, electrochemistry, IR, and NMR spectroscopy without any additional purification. Any generated H₂S was quenched by bubbling it through a bleach or lead(II) chloride solution.

NMR spectra were collected on a Bruker AVIII-400 MHz or Bruker DRX-600 MHz spectrometer using CDCl₃ as the solvent. ¹H NMR chemical shifts (δ) are reported in ppm (CHCl₃: δ = 7.26 ppm for ¹H). All IR spectra were collected using a Thermo Nicolet Avatar ESP 380 FT-IR spectrometer using the OMNIC version 7.3 software. Samples were dissolved in CH₂Cl₂ or hexanes and placed between two NaCl plates in an air-free IR cell. UV-visible spectra were collected on an Ocean Optic spectrophotometer. Figures were prepared using WinFp v. 22.09 written by Prof. Dennis L. Lichtenberger.

Preparation of 4,5-bis-(hydroxythiophene-2-yl-methyl)-[1,3]dithiole-2-thione, 10⁵¹

0.90 M lithium diisopropylamide (LDA) was prepared by freeze-pump-thawing diisopropylamine (0.75 mL, 5.4 mmol) in dry tetrahydrofuran (1.88 mL) in a Schlenk flask to remove oxygen from the solution. This solution was then cooled to -78 °C, and *n*-butyllithium in hexanes (3.37 mL, 1.6 M) was syringed in and kept at -78 °C with stirring until ready for use. In a round bottom flask vinylene trithiocarbonate (0.201 g, 1.49 mmol) was dissolved in tetrahydrofuran (5 mL) and cooled to -78 °C. To this solution the previously prepared LDA solution (2.00 mL, 1.8 mmol) was added and stirred for 20 min after which time the thiophene-2-carboxaldehyde (0.139 mL, 1.5 mmol) was added and the mixture was left to stir for an additional 10 min. A second addition of LDA (2.00 mL, 1.8 mmol) was added and stirred for 20 min after which time a second addition of thiophene-2-carboxaldehyde (0.139 mL, 1.5 mmol) was added and the mixture was stirred for another 10 min. The reaction mixture was then allowed to warm ambiently to room temperature with stirring for an additional 1.5 h. Saturated aqueous sodium bicarbonate (20 mL) was added and the organic phase was removed. The aqueous phase was washed with dichloromethane (3 x 20 mL) and the combined organic extracts were washed once with brine and then dried over anhydrous MgSO₄. The solvent was removed under reduced pressure and the product was isolated by column chromatography (silica, dichloromethane/ethyl acetate (9:1 v/v)) to afford the product as an orange-red oil (0.163 g), and used immediately in the next step as it was previously reported to be unstable.⁵¹

Preparation of [5-(thiophene-2-carbonyl)-2-thioxo-[1,3]dithiol-4-yl]thiophene-2-yl-methanone, **11⁵¹**

10 (0.163 g, 0.454 mmol) was dissolved in dichloromethane (8 mL) in a scintillation vial. To this was added MnO₂ (10 × excess w/w, 1.630 g), prepared according to previously reported literature,⁵² portionwise and stirred overnight. The solution was filtered through a silica plug eluting with dichloromethane until no more color was observed. The solvent was removed under reduced pressure to afford **11** as a yellow oil. ¹H NMR (CDCl₃) δ 7.72 (dd, *J* = 1.1 and 4.9 Hz, 2H), 7.71 (dd, *J* = 1.1 and 3.9 Hz, 2H), 7.10 (dd, *J* = 3.9 and 4.9 Hz, 2H).

Preparation of 4,5-bis(thiophene-2-carbonyl)[1,3]dithiole-2-one, **12⁵¹**

To a solution of **11** (0.105 g, 0.296 mmol) in dichloromethane/glacial acetic acid (3:1 v/v, 2.67 mL) was added mercuric acetate (0.132 g, 0.416 mmol). The resulting mixture was stirred at room temperature for 16 h and was gravity filtered the following day, washing with dichloromethane. The organic eluent was washed with water (3 × 20 mL), saturated aqueous sodium bicarbonate solution (3 × 20 mL), dried over anhydrous MgSO₄, and then filtered. The solvent was removed under reduced pressure to afford **12** as an off-white, almost green colored, solid (0.244 g, 85%). ¹H NMR (CDCl₃) δ 7.71 (dd, *J* = 1.1 and 4.9 Hz, 2H), 7.68 (dd, *J* = 1.1 and 3.9 Hz, 2H), 7.09 (dd, *J* = 3.9 and 4.9 Hz, 2H).

Preparation of 4,6-di-thiophene-2-yl-thieno[3,4-*d*][1,3]dithiol-2-one, **13⁵¹**

In a two-neck round bottom flask with condenser, a mixture of **12** (41 mg, 0.122 mmol), sodium bicarbonate (41 mg, 0.492 mmol), and diphosphorus pentasulfide (0.125 g, 0.565 mmol) was stirred in 1,4-dioxane (1 mL). The reaction mixture was heated to 90 °C, held there for 3 h, and then cooled to room temperature. Water (7.5 mL) was added to the mixture (CAUTION! H₂S and CO₂ evolution) and stirred overnight. The mixture was filtered, washed with water, and dried

by vacuum filtration. This solid was then dissolved in hot chloroform and filtered to remove insoluble solids, resulting in an orange colored solution. The solvent was removed under reduced pressure, and **13** (32 mg, 77%) was obtained as an orange solid. $^1\text{H NMR}$ (CDCl_3) δ 7.38 (dd, $J = 1.1$ and 5.1 Hz, 2H), 7.24 (dd, $J = 1.1$ and 3.7 Hz, 2H), 7.11 (dd, $J = 3.7$ and 5.1 Hz, 2H). MS (MALDI) m/z : 338 (M^+ , 6%), 310 ($\text{M}^+ - \text{CO}$, 100%).

Preparation of (2,5-bis-(2',2''-thiophen-2-yl)-thiophene- μ -3,4-dithiolato)diiron hexacarbonyl, **1 (terthiophene-cat)**

In a round bottom flask with a condenser attached was dissolved **13** (0.101 g, 0.298 mmol) and $\text{Fe}_2(\text{CO})_9$ (0.433 g, 1.190 mmol) in dry toluene (3 mL). This mixture was heated to $70\text{ }^\circ\text{C}$ for 1 h and then cooled to room temperature. The solvent was removed under reduced pressure, and the product was isolated by column chromatography (silica, hexanes/benzene (19:1 v/v)) to afford **1** as a dark red solid (95 mg, 54%). $^1\text{H NMR}$ (CDCl_3) δ 7.35 (dd, $J = 1.1$ and 5.1 Hz, 2H), 7.32 (dd, $J = 1.1$ and 3.7 Hz, 2H), 7.04 (dd, $J = 3.7$ and 5.1 Hz, 2H); $^{13}\text{C NMR}$ (CDCl_3) δ 207.2, 140.9, 134.0, 130.5, 127.7, 126.4, 126.3; IR (hexanes) ν/cm^{-1} : 2078, 2046, 2008, 2006; UV-vis (CH_2Cl_2) λ/nm : 339, 431.

Computational methodology

Computational methodology has previously been described for systems containing a diiron disulfur-bridged core.⁵³ The computational values were validated by computations capability to account for the structures, carbonyl stretching frequencies, oxidation and reduction potentials and other electrochemical parameters, and the metal-metal and metal-ligand bond energies. All computations were performed using ADF2012.01.⁵⁴⁻⁵⁶ Geometry optimizations and frequency calculations were performed using LDA VWN STOLL.⁵⁷ The OPBE⁵⁸ density functional was used to calculate electronic energies as previous studies have shown OPBE to be a good model for iron

containing systems.⁵⁹ All calculations were performed using the TZP basis set. Relativistic effects were taken into account in all calculations using the scalar ZORA formalism.⁶⁰ All electronic structures with unpaired spins were calculating using an unrestricted framework. The computational gas-phase metal-carbonyl stretching frequencies were scaled by a factor of 0.38% to allow comparison to experimental values. Solvation effects on the complex was modeled through the Conductor-like Screening Model (COSMO) of solvation.⁶¹ The solvent parameters implemented were those defined by the ADF2012.01 program to simulate a dichloromethane solvated environment. Free energy (G) values were calculated from the electronic self-consistent-field (SCF) energies considering the $q_{\text{translational}}$, $q_{\text{rotational}}$, and $q_{\text{vibrational}}$ contributions⁶² and the enthalpy and entropy terms were calculated under STP conditions.

Electrochemistry

The electrochemical studies presented in this thesis were performed using a Gamry Instruments Reference 3000 and were collected at the University of Arizona. Potentials are reported versus the potential of the ferrocinium/ferrocene couple measured in dichloromethane. All cyclic voltammetry experiments were performed at room temperature in a degassed solution of dichloromethane containing 0.20 M Bu₄NPF₆ on a glassy carbon working electrode (GCE) under a dichloromethane saturated Ar atmosphere to minimize solvent evaporation. Approximately 0.1 mM solutions of the compounds were used in each experiment.

Single-crystal X-ray diffraction

Single-crystal X-ray diffraction data was measured on a Bruker Kappa APEX-II DUO diffractometer with graphite-monochromated MoK α radiation ($\lambda = 0.71073 \text{ \AA}$) and a crystal temperature of 100 K in the X-ray Diffraction Facility in the Department of Chemistry and Biochemistry. **1** was collected by Gabriel B. Hall. The structure was solved using Olex2⁶³ with the

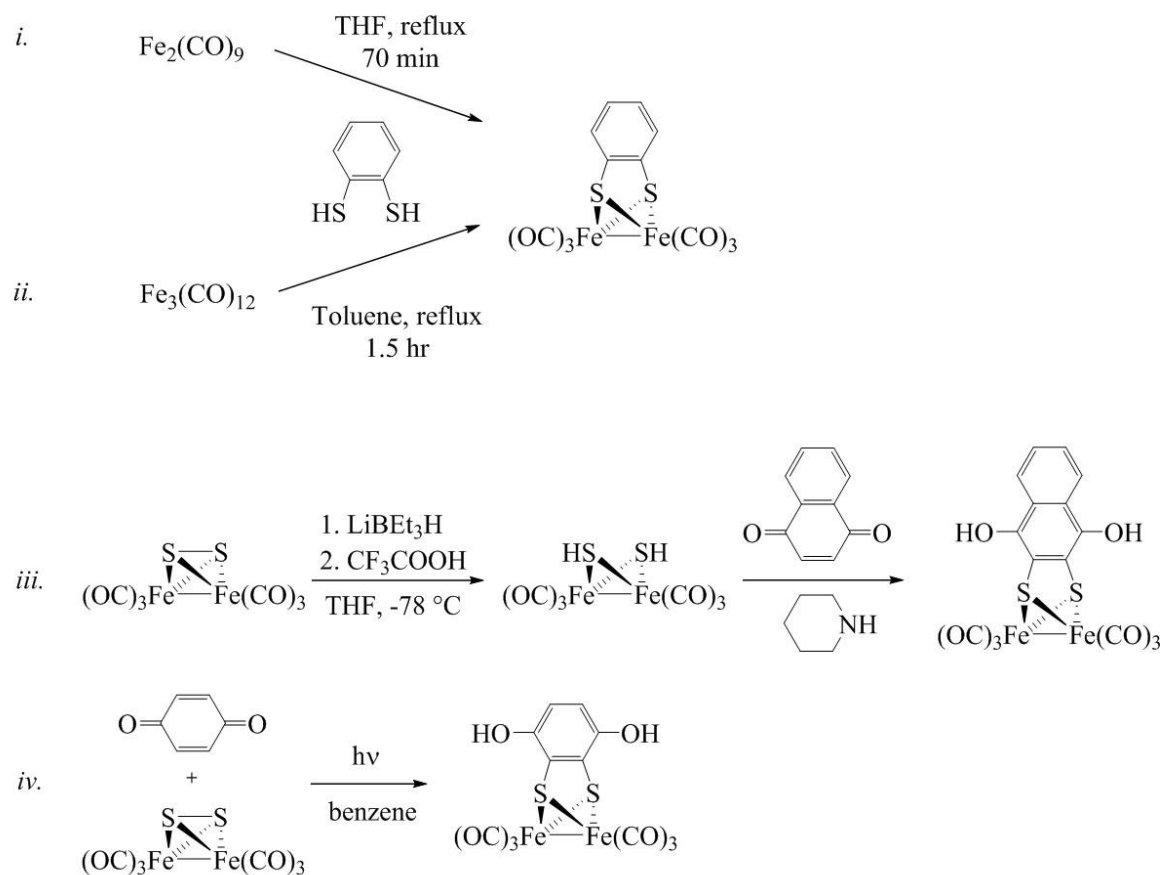
XM⁶⁴ structure solution program using Dual Space and refined with the XL⁶⁴ refinement package using Least Squares minimization.

Chapter 3 : SYNTHESIS OF (2,5-BIS-(2',2''-THIOPHEN-2-YL)-THIOPHENE- μ -3,4-DITHIOLATO)DIIRON HEXACARBONYL

Introduction

Synthesis of [FeFe]-hydrogenase active site mimics with novel ligand architecture is valuable for the study of molecular hydrogen production by this class of complexes. Prior to undertaking synthesis of a new complex, such as **1**, it is important to understand the methodologies which have been employed for similar systems. For the [FeFe]-hydrogenase mimics that have an aryl system bridging the 2Fe2S core of the catalyst, such as (μ -1,2-benzenedithiolato)diiron hexacarbonyl (**2**) and (μ -1,2-thiophenedithiolato)diiron hexacarbonyl (**3**), there are several synthetic routes that can be implemented.⁶⁵⁻⁷⁰ In these synthetic routes, the [FeFe]-hydrogenase mimic is synthesized from the direct reaction between a dithiol and either diiron nonacarbonyl ($\text{Fe}_2(\text{CO})_9$)^{65,68} or triiron dodecacarbonyl ($\text{Fe}_3(\text{CO})_{12}$),^{66,69} or by reacting (μ -disulfide)diiron hexacarbonyl ($\text{Fe}_2\text{S}_2(\text{CO})_6$) with a reducing reagent, such as LiBEt_3H , followed by addition of an acid, CF_3COOH , and a quinone, such as 1,4-naphthoquinone catalyzed by pyrrolidine,⁶⁷ or through irradiation of $\text{Fe}_2\text{S}_2(\text{CO})_6$ and 1,4-benzoquinone,⁶⁷ as shown in Scheme 3.1.

Of these synthetic pathways, the simplest is through the direct reaction of an aryl dithiol with $\text{Fe}_2(\text{CO})_9$ (pathway *i*) or $\text{Fe}_3(\text{CO})_{12}$ (pathway *ii*) in either tetrahydrofuran (THF) or toluene at reflux conditions. After removal of the solvent, the product can then be purified by column chromatography, with yields reported between 18-45% when using $\text{Fe}_2(\text{CO})_9$,^{65,68} and 15-57% with $\text{Fe}_3(\text{CO})_{12}$.^{66,69} However, if compound stability is an issue on the column, then recrystallization or sublimation can be implemented. A drawback to this method, however, is that the aryl dithiol compound must be readily accessible through synthetic methods or commercially available. If neither is possible, then this synthetic route cannot be used. The third method involves the dithiol being generated at the metal center, followed by the reaction with the aromatic



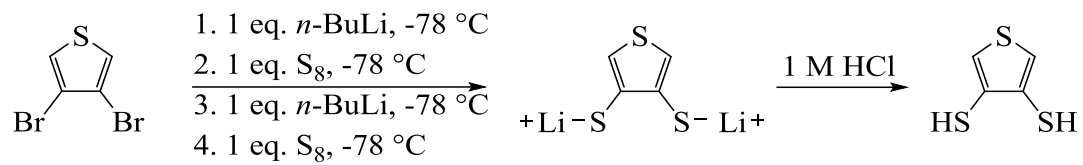
Scheme 3.1. *i.* Reaction of $\text{Fe}_2(\text{CO})_9$ with 1,2-benzenedithiol. *ii.* Reaction of $\text{Fe}_3(\text{CO})_{12}$ with 1,2-benzenedithiol. *iii.* Reaction $\text{Fe}_2\text{S}_2(\text{CO})_6$ with superhydride and trifluoroacetic acid to produce the $\text{Fe}_2(\text{SH})_2(\text{CO})_6$ intermediate, and the following reaction with 1,4-naphthoquinone and piperidine. *iv.* Reaction with 1,4-benzoquinone and $\text{Fe}_2\text{S}_2(\text{CO})_6$ in benzene using irradiation.

compound. For this route to be viable, a conjugate addition of the dithiol across the carbon-carbon double bond of the quinone ring must occur (pathway *iii*), followed by an oxidation to allow the second addition to proceed.⁶⁷ The last method involves harsh conditions in which the mixture is irradiated to initiate a reaction between $\text{Fe}_2\text{S}_2(\text{CO})_6$ and the quinone (pathway *iv*). Unfortunately, this last method is a low yielding reaction compared to the others.⁶⁷ Generation of **1** was attempted through the direct reaction of pathways *i* and *ii*, by trying to design the aromatic thiophene, **14**, which is similar to 3,4-thiophenedithiol. However, the desired compound was not obtained, and to overcome this drawback, a different ligand, 4,5-di-thiophen-2-yl-thieno[3,4-*d*][1,3]dithiol-2-one (**13**) was synthesized, and was found to produce (2,5-bis-(2',2''-thiophen-2-yl)-thiophene- μ -3,4-dithiolato)diiron hexacarbonyl (**1**) via a direct reaction with $\text{Fe}_2(\text{CO})_9$ in toluene in a 54% yield.

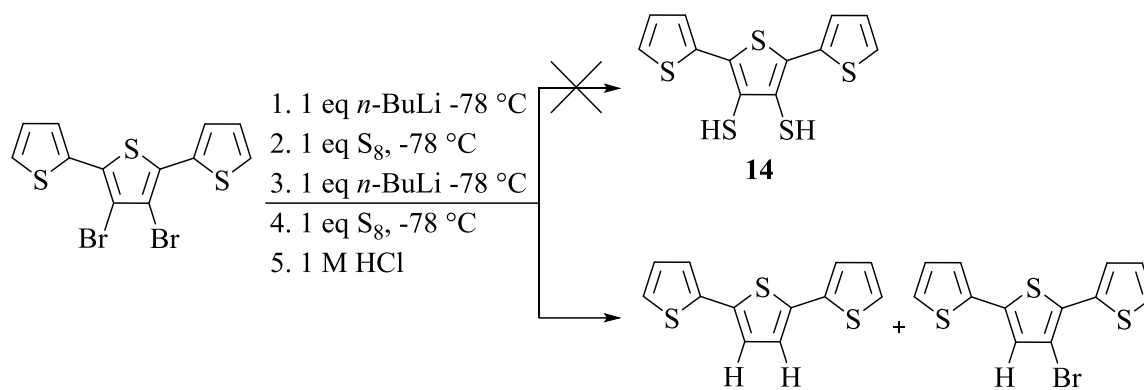
Results and Discussion

(2,5-bis-(2',2''-thiophen-2-yl)-thiophene- μ -3,4-dithiolato)diiron hexacarbonyl.

The initial route to synthesize **1** was investigated through the 2,5-bis(2',2''-thiophen-2-yl)-3,4-thiophenedithiol, **14**, which is not a commercially available aryl dithiol. The work reported by Cowan et al.,⁷¹ Scheme 3.2, was used as a model synthesis for **14**, wherein the authors synthesized dilithium 3,4-thiophenedithiolate from 3,4-dibromothiophene by two consecutive one equivalent additions of *n*-butyllithium and sulfur. Addition of a dilute acid to this intermediate product was found to produce 3,4-thiophenedithiol in about a 50% yield based on ¹H NMR spectroscopic analysis.³² In place of 3,4-dibromothiophene, 3,4-dibromo-2,2':5',2''-terthiophene was used to synthesize **14**, which was synthesized according to literature methods,⁷² shown in the top route of Scheme 3.3. After the additions of *n*-butyllithium and sulfur, the reaction mixture changed color from yellow to orange, following a similar green to yellow color change trend observed with the less conjugated 3,4-dibromothiophene.⁷¹ However, after acidification of the reaction mixture and



Scheme 3.2. Synthetic route of lithium 3,4-thiophenedithiolate (middle) followed by protonation to the 3,4-thiophenedithiol (right).



Scheme 3.3. Proposed synthesis for preparing **14** (top) which failed, and the major products obtained (bottom) from the reaction.

isolation of the products via column chromatography, eluting with pentane, none of the desired compound **14** was collected. The major products obtained after isolation, bottom route of Scheme 3.3, were characterized by ^1H NMR spectroscopy and were found to be terthiophene, isolated as a white solid, and the mono-brominated terthiophene, isolated as an oily yellow solid that matched previously reported ^1H NMR spectroscopic data.⁷³ The lack of any mono or dithiol product being observed after isolation suggests that there is no reaction occurring between the sulfur and carbanion intermediate under the conditions used.

With the desired dithiol product not being generated from the synthetic method shown in Scheme 3.3 above, an alternate pathway was pursued involving work published by Skabara et al. to synthesize 4,5-di-thiophen-2-yl-thieno[3,4-*d*][1,3]dithiol-2-one (**13**).⁵¹ The synthesis of **13** was achieved through the multi-step synthesis described previously in Chapter 2,⁵¹ and as shown in Scheme 3.4 with each step producing moderate to good yields of the respective product. After isolation, **13** (101 mg, 0.298 mmol) was then reacted with $\text{Fe}_2(\text{CO})_9$ (433 mg, 1.190 mmol) in dry toluene and heated to 70 °C, as shown in Scheme 3.5.⁷⁴ The reaction mixture turned to a dark red color as it was heated, and bubbles appeared from the solution as the temperature of the oil bath reached 70 °C, indicating a reaction between **13** and $\text{Fe}_2(\text{CO})_9$. To track the progress of this reaction, infrared spectroscopy was used to monitor the carbonyl stretching frequency region, shown in Figure 3.1. The appearance of a new set of peaks observed forty minutes into the reaction in the 2100-2000 cm^{-1} region were attributed to a new compound in solution, and a decrease in the peaks corresponding to $\text{Fe}_2(\text{CO})_9$ was observed just prior to an hour in the reaction. After the solvent was removed by rotary evaporation, column chromatography was performed to isolate the product by eluting through silica gel with a mixture of hexanes and benzene (19:1 v/v). On the column, the product was observed as an orange-red colored band that was preceded by separate

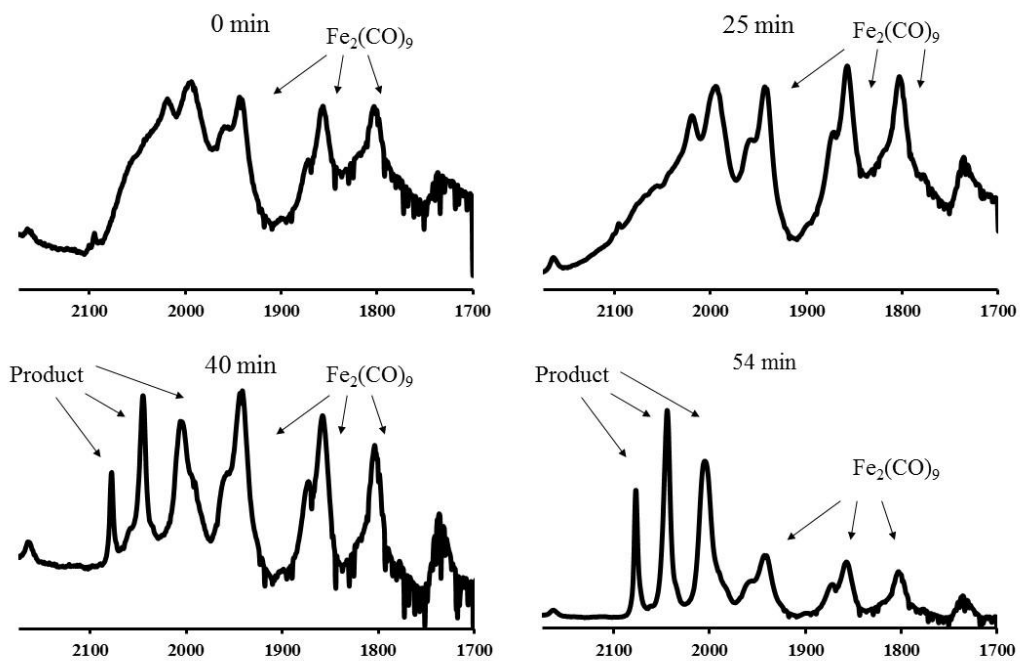
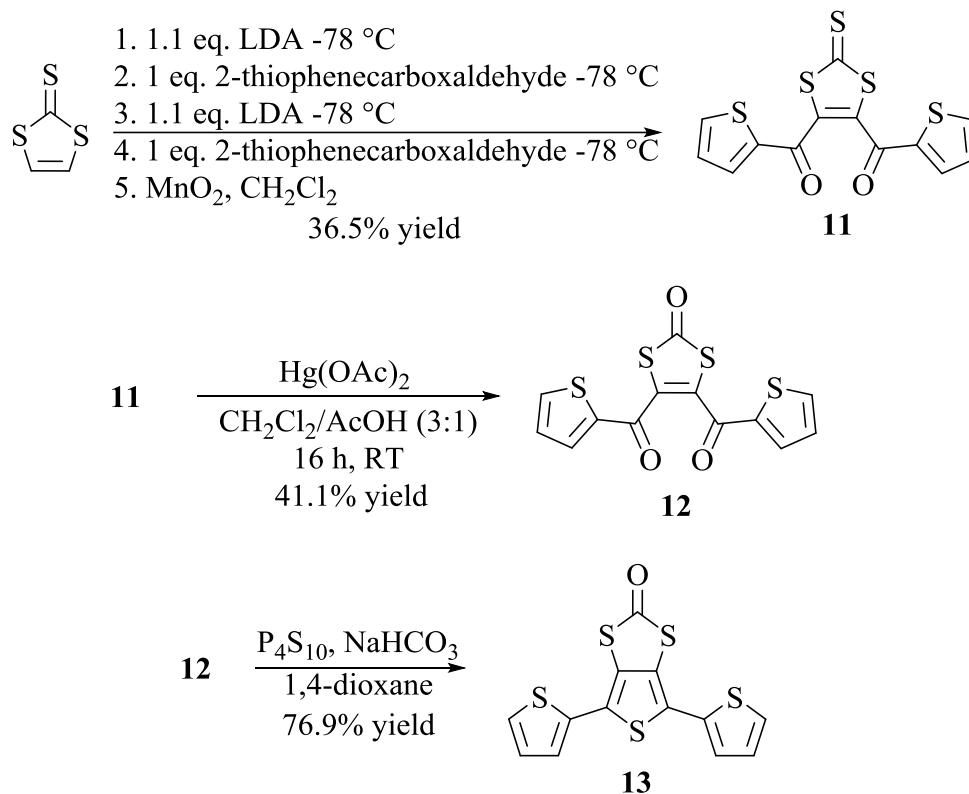
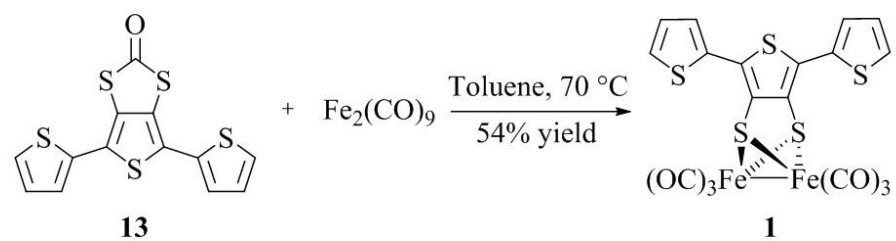


Figure 3.1. Infrared spectroscopy of the carbonyl stretching frequency region (wavenumbers, cm^{-1}) collected to track the reaction progress of **13** with $\text{Fe}_2(\text{CO})_9$ in toluene.



Scheme 3.4. *Top:* Synthesis of **11** from vinylene trithiocarbonate and two consecutive additions of lithium diisopropylamide (LDA) and 2-thiophenecarboxaldehyde, followed by oxidation of the intermediate product with MnO₂. *Middle:* Conversion of the trithiocarbonate to the dithiocarbonate, **12**. *Bottom:* Ring closure reaction using P₄S₁₀ and NaHCO₃ in 1,4-dioxane.



Scheme 3.5. Synthesis of complex **3**.

green and yellow colored bands. The orange-red colored band was collected and the solvent was removed by rotary evaporation, leaving 95 mg (54% yield) of **1**, a red colored solid, in the flask. The product was determined to be unstable, based on a ^1H NMR spectra taken three days after the product was isolated which had very broad, undefined peaks, indicating that a paramagnetic compound had formed after **1** was exposed to light under non-inert conditions. The decomposed material was removed by filtering through a small silica pad, and the resulting solution had a clean ^1H NMR spectra with better resolved peaks, with roughly 80% of the pure material collected back after isolation.

Conclusion

It has been shown that the synthesis of (2,5-bis-(2',2''-thiophen-2-yl)-thiophene- μ -3,4-dithiolato)diiron hexacarbonyl, **1**, is possible through the direct reaction of the dithiolcarbonate, **13**, with $\text{Fe}_2(\text{CO})_9$. Using this alternative reaction, **1** was synthesized in 54% yield, which is comparable to similar methods that react an aryl dithiol directly with $\text{Fe}_2(\text{CO})_9$,^{65,70} or $\text{Fe}_3(\text{CO})_{12}$,⁶⁶ to generate [FeFe]-hydrogenase mimics. This is also a better and more successful method for producing **1** than the method reported for **3** wherein 3,4-thiophenedithiol is synthesized as the precursor.³² This type of reaction will be useful for synthesizing new [FeFe]-hydrogenase mimics where the dithiol precursor required cannot be purchased or synthesized through conventional methods.

Chapter 4 : CHARACTERIZATION OF (2,5-BIS-(2',2''-THIOPHEN-2-YL)-THIOPHENE- μ -3,4-DITHIOLATO)DIIRON HEXACARBONYL

Introduction

Characterization of the [FeFe]-hydrogenase mimics is obtained through well-known techniques such as of infrared (IR) spectroscopy, X-ray crystallography, nuclear magnetic resonance (NMR) spectroscopy, and UV-visible absorption spectroscopy. Infrared spectroscopy of the metal carbonyl stretching frequency region provides a determination of the electronic density at the metal center, as the CO ligand is a well-known reporter ligand due to the sensitivity of the stretching frequency to the metal's electron density. Additionally, the general symmetry of the complex can be determined based on the number of stretching frequencies observed and their relative intensities. Use of X-ray crystallography provides an exact representation of the structure of the complex in the solid state and can be used to determine if the correct compound was synthesized, while NMR spectroscopy provides information about the electronic and chemical environment that each unique NMR active nucleus is in based on the chemical shift (ppm) and the coupling constant, J (Hz). Lastly, for UV-visible spectroscopy, the electronic transitions of the complex can be found based on the λ_{max} for each peak, along with the molar extinction coefficient (ϵ) which provides information about the type of transition. Combining all of these techniques allows for the determination of the structural and electronic properties of a complex.

Nuclear Magnetic Spectroscopy

The synthesis of (2,5-bis-(2',2''-thiophen-2-yl)-thiophene- μ -3,4-dithiolato)diiron, **1**, hexacarbonyl was achieved through the reaction of **13** and $\text{Fe}_2(\text{CO})_9$ in toluene at 70 °C and was purified by column chromatography as described in the Experimental Chapter. The ^1H , ^{13}C , heteronuclear single quantum correlation (HSQC), and heteronuclear multiple bond correlation (HMBC) NMR spectra of **1** were collected in CDCl_3 , and are shown below in Figures 4.1, 4.2, 4.3,

and 4.4 with all of the assignments compiled in Table 4.1. The ^1H NMR displayed three unique peaks in the proton aromatic region with chemical shifts observed at 7.35 ppm for H_1 , 7.32 ppm for H_2 , and 7.04 ppm for H_3 , as shown in Figure 4.1, for the three protons. The proton assignments were determined based on the analysis of the HSQC and HMBC spectrum in Figures 4.3 and 4.4, respectively. The chemical shifts observed for H_1 and H_2 are located in the middle of the proton aromatic region, indicating that there is little to no electron withdrawing effect from the $2\text{Fe}_2\text{S}_2$ core due to the carbonyl ligands, nor is there an electron donating effect into the terthiophene ring from the bridging sulfurs. As for the upfield chemical shift observed for H_3 , this can be attributed to resonance within the thiophene ring inducing an increased electron density at this position.

These absorption peaks were all doublet of doublets, indicating that each pair of protons on the pendant thiophene rings are chemically equivalent and are coupled only with the neighboring hydrogen atoms on the respective thiophene ring. From these peaks, the coupling constants were determined to be 5.1 and 1.1 Hz for H_1 , 3.7 and 1.1 Hz for H_2 , and 5.1 and 3.7 Hz for H_3 . As there are only three unique J values, this further indicates that there are only three chemically and magnetically unique protons in **1**. The peaks corresponding to protons H_1 and H_2 contain the 1.1 Hz J coupling value, indicating that these two protons are coupled to each other, while proton H_3 is coupled separately to H_1 and H_2 through the respective 5.1 and 3.7 Hz coupling constants.

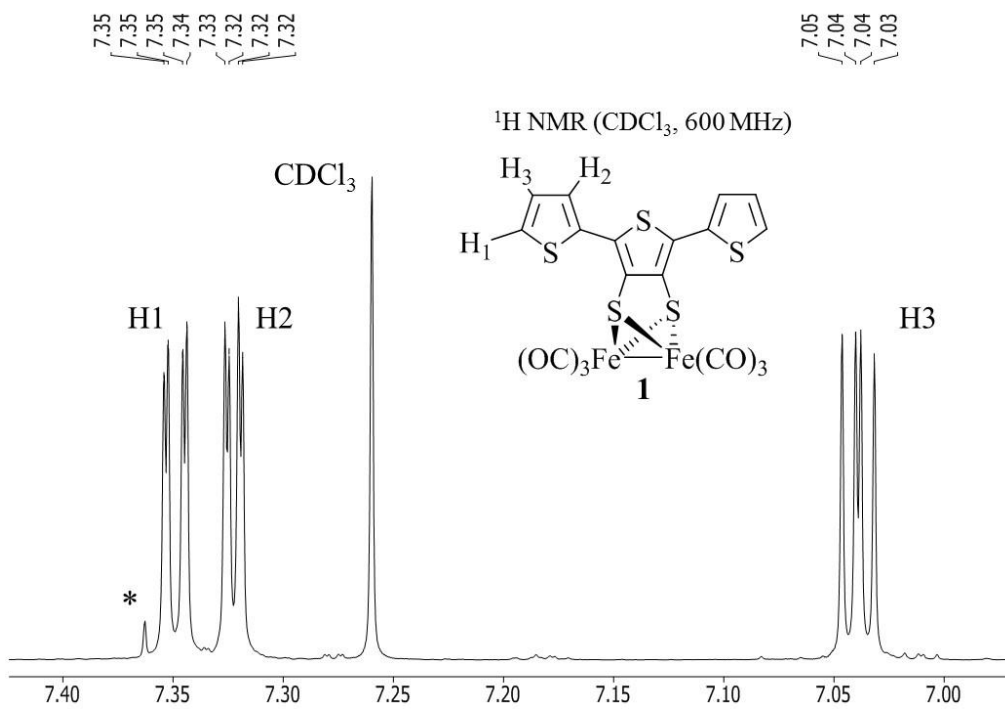


Figure 4.1. ^1H NMR spectrum of **1** in CDCl_3 . Residual benzene solvent absorption is indicated with the asterisk.

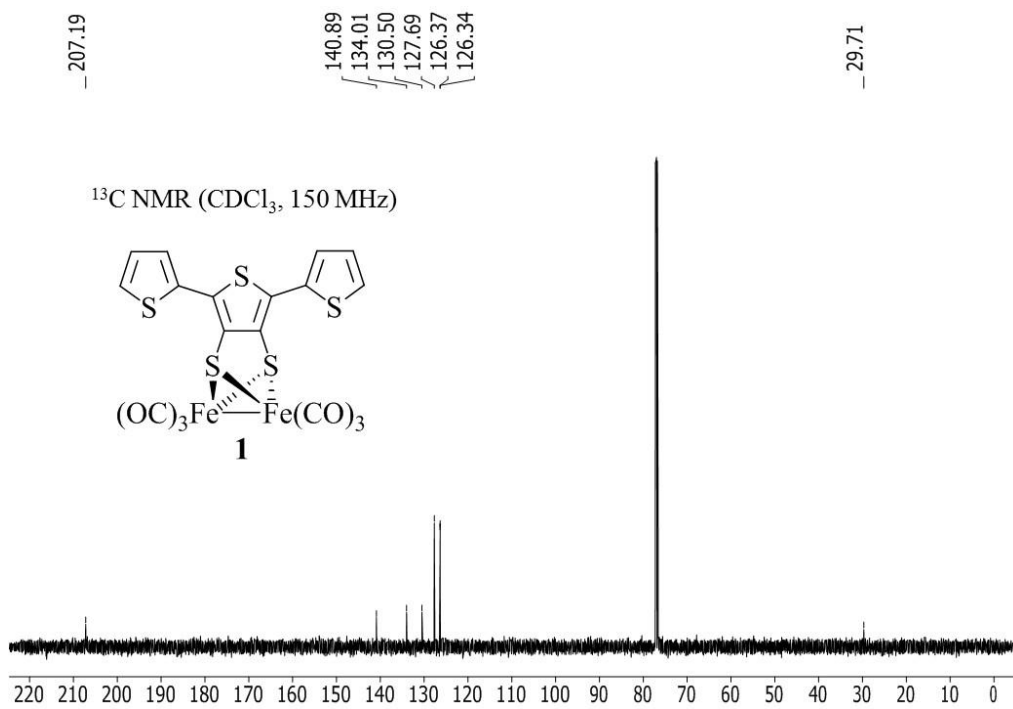


Figure 4.2. ^{13}C NMR of **1** in CDCl₃.

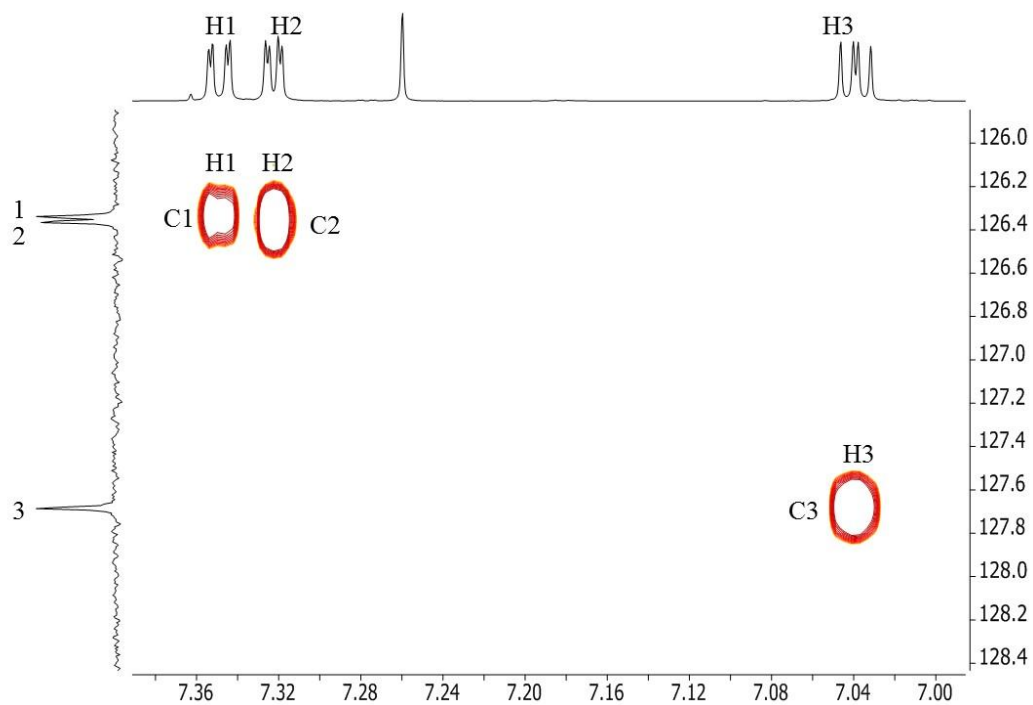


Figure 4.3. Heteronuclear Single Quantum Correlation (HSQC) NMR spectroscopy of **1** in CDCl_3 . ^1H NMR spectrum is displayed on the horizontal axis and the ^{13}C NMR spectrum is displayed on the vertical axis.

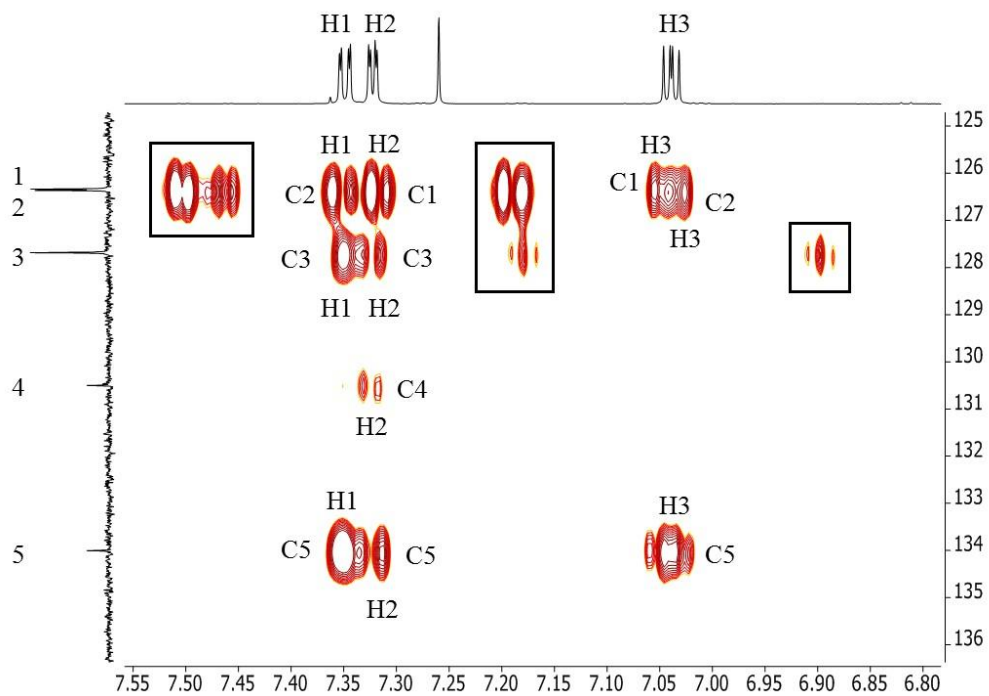


Figure 4.4. Heteronuclear Multiple Bond Correlation (HSQC) NMR spectroscopy of **1** in CDCl_3 . ^1H NMR spectrum is displayed on the horizontal axis and the ^{13}C NMR spectrum is displayed on the vertical axis. The boxed peaks are artifact $^1J_{\text{CH}}$ couplings.

Table 4.1. 1D and 2D NMR assignment of **1** in CDCl₃.

Number	¹ H ppm	Integral	Mult	<i>J</i>	¹³ C ppm	Type	HMBC
1	7.35	2	dd	5.1, 1.1	126.3	CH	c2,3,5
2	7.32	2	dd	3.7, 1.1	126.4	CH	c1,3,4,5
3	7.04	2	dd	5.1, 3.7	127.7	CH	c1,2,5
4	----	----	----	----	130.5	C _q	----
5	----	----	----	----	134.0	C _q	----
6	----	----	----	----	140.9	C _q	----
7	----	----	----	----	207.2	CO	----

Infrared Spectroscopy: CO stretching frequency

The electron density on a metal can be characterized through the CO stretching frequency values (ν -CO), as CO is a well-known reporting ligand for determining the electronic character on the metal. The ν -CO stretching frequencies in the infrared region for **1** is shown in Figure 4.5 and is compared with the experimental frequencies observed for **2** and **3**. Figure 4.5 shows that there is very little deviation in the experimental ν -CO stretching frequencies, indicating that the electronic character at the irons in these three complexes is not appreciably altered when the bridging aryl dithiol is changed from the 1,2-benzenedithiol to the 3,4-thiophenedithiol or the 2,5-bis-2',2''-thiophen-2-yl-3,4-thiophenedithiol. One noticeable difference observed between the three different spectra is that **1** has two ν -CO peaks at 2008 and 2006 cm^{-1} while **2** and **3** have only one peak at 2006 and 2007 cm^{-1} , respectively. This observation may be due to a perturbed geometry of **1** in solution that causes an energy separation between the two CO stretching frequency peaks significant enough to allow isolation of the peaks. Figure 4.2 also shows a relative lowering of the intensity of this set of peaks for **1** compared to the single peak for **2** and **3** at around 2007 cm^{-1} . This indicates that there are two overlapping peaks at this vibrational energy for **2** and **3**, but the instrument resolution is not adequate enough to individually isolate the different peaks. Whereas in **1**, a perturbed geometry to the multiple conformers in solution may be causing the splitting of the single peak into two separate peaks.

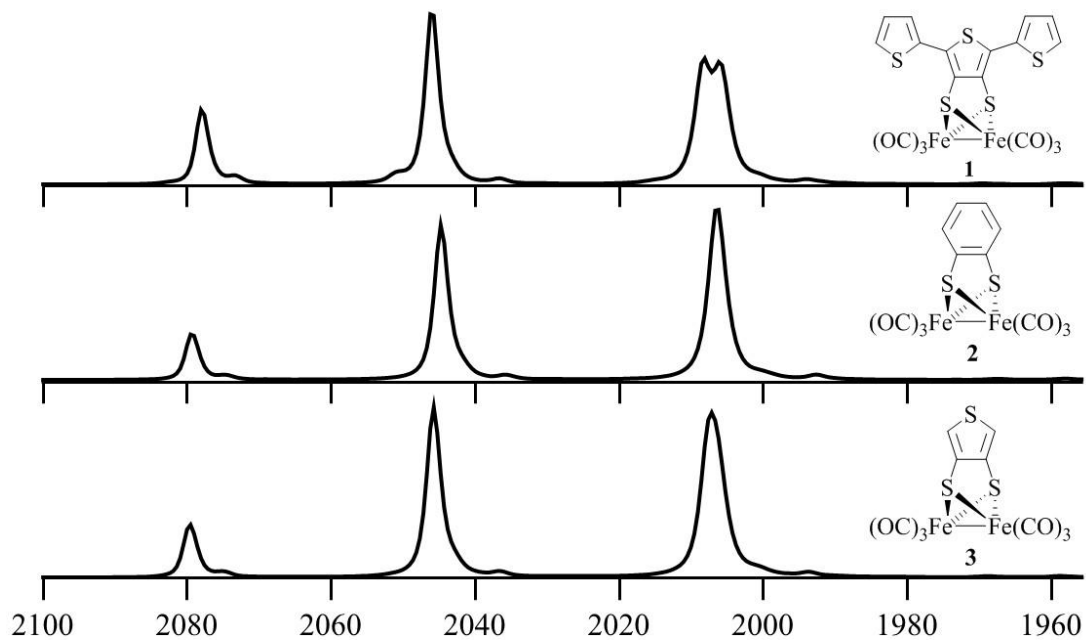


Figure 4.5. Comparison of the experimental IR spectra in the carbonyl stretching frequency region for **1**, **2**, and **3**. All spectra were collected in hexanes using an air-free IR cell.

X-Ray Crystal Structure

The structure of **1** was determined by X-ray crystal diffraction, and the experimental parameters are shown below in Table 4.1. Selected bond lengths and angles for **1** are listed in Table 4.2 below. From the X-ray crystallographic data, **1** was found to have crystallized in a monoclinic space group of $P2_1/n$. The torsion angle observed for the two thiophenes that are connected to the central thiophene is not zero degrees, but rather 176.0 and -171.9 degrees for S4-C14-C15-S5 and S4-C11-C10-S3, respectively, using the labeling scheme shown in Figure 4.6. This twist away from a completely planar terthiophene ligand creates the asymmetry that is observed in the crystal structure and lowers the overall symmetry of the molecule to C_1 which could be an effect caused by the crystal packing. And as was shown above in the IR absorption section, there is a fourth CO stretching frequency peak observed for **1** but not **2** or **3**, that may be present due to a decrease of symmetry of **3** in solution due to a perturbed geometry of the complex.

The same selected bond lengths and angles for **2** and **3** are listed in Table 4.3 for comparison to **1**. The listed values show that there is a large similarity between the bond lengths and angles in these three complexes. A couple very minor differences are seen in the Fe-Fe bond lengths that differ by only 0.0089 Å between **1** and **2**, and 0.0139 Å between **1** and **3**. The S...S atom distance is also similar between **1** and **3**, varying by only 0.009 Å, and **2** having the shortest bond distance. Consequently, as the S...S atom distance increases, the S-Fe-S angle also increases, due to the bond angle opening up as the sulfurs are pushed further apart. A similar trend is observed with the Fe-S bond as the bond length increases with the same trend observed as the increasing S...S atom distance separation.

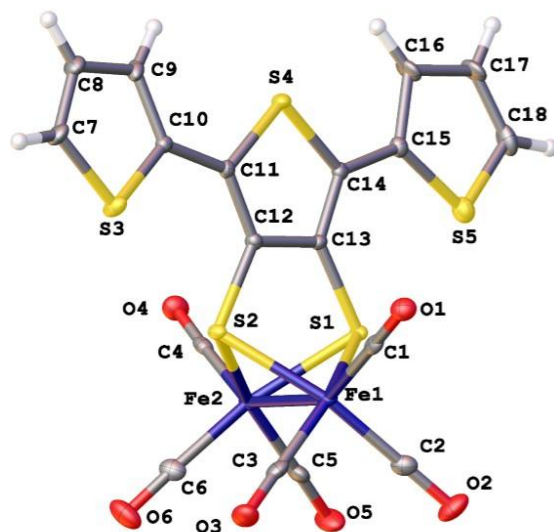


Figure 4.6. Thermal ellipsoid plot of **1** obtained by X-ray crystal diffraction with thermal ellipsoids at the 50% probability level.

Table 4.2. X-ray crystallographic parameters for **1**.

Empirical formula	$C_{18}H_6Fe_2O_6S_5$
Formula weight	590.23
Temperature/K	100
Crystal system	monoclinic
Space group	$P2_1/n$
$a/\text{\AA}$	7.2294(10)
$b/\text{\AA}$	21.611(3)
$c/\text{\AA}$	14.0228(13)
$\alpha/^\circ$	90.00
$\beta/^\circ$	104.842(4)
$\gamma/^\circ$	90.00
Volume/ \AA^3	2117.8(4)
Z	4
$\rho_{\text{calc}}/\text{mg}/\text{mm}^3$	1.851
m/mm^{-1}	1.897
F(000)	1176.0
Crystal size/ mm^3	$0.376 \times 0.308 \times 0.096$
2Θ range for data collection	3.54 to 52.72°
Index ranges	$-7 \leq h \leq 9, -26 \leq k \leq 27, -17 \leq l \leq 17$
Reflections collected	15152
Independent reflections	4314[R(int) = 0.0280]
Data/restraints/parameters	4314/0/274
Goodness-of-fit on F^2	1.031
Final R indexes [$I \geq 2\sigma(I)$]	$R_1 = 0.0345, wR_2 = 0.0861$
Final R indexes [all data]	$R_1 = 0.0444, wR_2 = 0.0922$
Largest diff. peak/hole / $e \text{\AA}^{-3}$	1.29/-0.92

Table 4.3. Selected bond lengths and angles obtained from crystallographic data of **1**, **2**, and **3**.^a

Bond/Angle ^b	X-ray ^c		
	1	2	3
Fe-Fe	2.4889(7)	2.480 (2)	2.475 (3)
S••S	2.980(1)	2.940 (2)	2.989 (6)
S-C _L	1.766(3)	1.777 (6)	1.772 (2)
Fe-S	2.2766(8)	2.268 (2)	2.2784 (5)
Fe-C _a	1.811(3)	1.802 (7)	1.808 (2)
Fe-C _b	1.798(3)	1.787 (7)	1.802 (2)
C _a -O _a	1.135(4)	1.132 (9)	1.140 (2)
C _b -O _b	1.143(4)	1.136 (9)	1.138 (2)
Fe-S-Fe	66.28(2)	63.30 (6)	65.80 (1)
C _a -Fe-C _b	99.7(1)	99.9 (3)	100.80 (8)
C _b -Fe-C _b	90.3(1)	91.3 (3)	90.57 (8)
C _a -Fe-Fe	147.7(1)	149.0 (2)	148.55 (5)
C _b -Fe-Fe	103.0(1)	101.6 (2)	101.18 (6)
S-Fe-S	81.76(3)	80.81 (4)	81.98 (2)
S4-C14-C15-S5	176.0(2)	NA	NA
S4-C11-C10-S3	-171.9(2)	NA	NA

^aBond lengths are in Å, and angles and torsion angles are in degrees. ^bC_a refers to the apical CO in the local square-based pyramid geometry of each Fe, and C_b refers to the basal CO. C_L refers to the carbon atom attached to the sulfur atom; both distances were the same. ^cNumbers in parentheses denote error in the measurement of the last decimal place.

Ultraviolet-visible Spectroscopy

The compounds **1**, **2**, and **3** are all red-orange solids with similar electronic and geometric structures based on reported X-ray crystal structures and ν -CO values for each compound.^{32,65} One difference between these complexes, however, was observed in the UV-visible absorption spectra shown in Figure 4.7 below. In the figure, an absorption band for **1** and **3** is observed in the low energy ultraviolet region (~337 nm) that corresponds to a π - π^* transition within the thiophene ligands,⁵⁰ along with a broad absorption band with a strong extinction coefficient of 6500 (M cm)^{-1} in CH_2Cl_2 from 400-500 nm for **1** compared to the small absorption band observed for **3** at 461 nm. **2** is not displayed as it has been shown to have a similar absorption spectra as that of **3**.³² The blue shifted visible absorption peak observed for **1** is indicative of a charge-transfer band based on the large extinction coefficient observed (6500 (M cm)^{-1}). The UV-visible spectra of both catalysts were collected in solvents with varying dielectric constants (ϵ), pentane (2), tetrahydrofuran (8), dichloromethane (9), and ethanol (25) as the polarity of the solvent can have an effect on the energy of the charge-transfer band. The concentration, absorbance, and ϵ values for **1** and **3** are shown in Table 4.4. In the different solvents, the shift in the λ_{max} was very small for both compounds (ca. 2-3 nm) as shown in Figure 4.7 and Table 4.4, and no discernible trend was observed for the extinction coefficient in the different solvents.⁷⁵

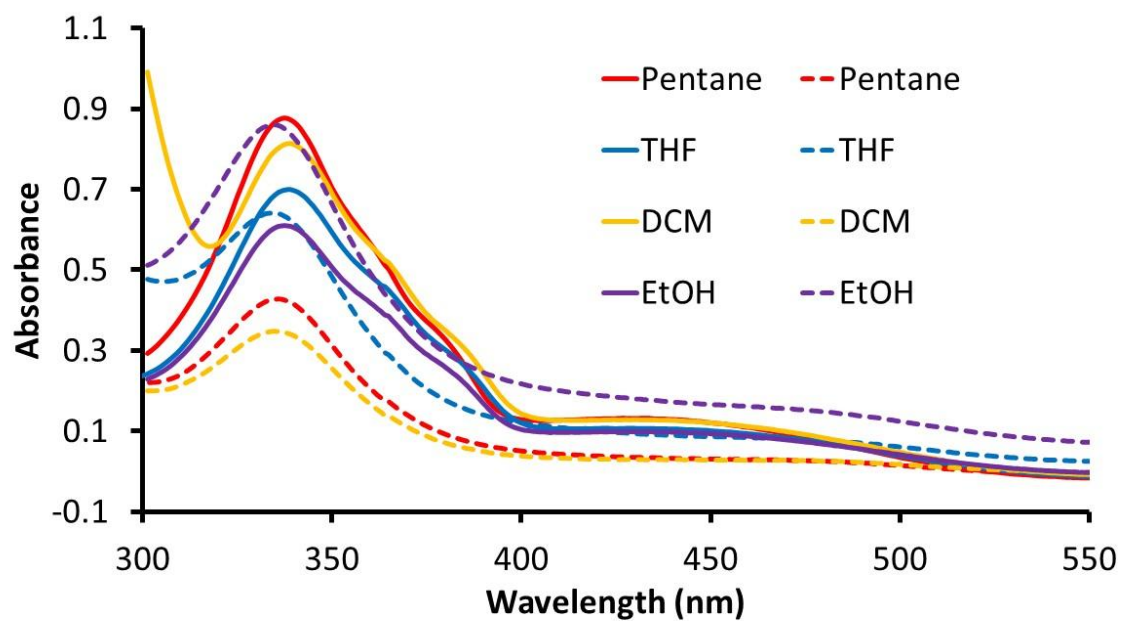


Figure 4.7. UV-visible absorption spectra comparison of **1** (solid line) and **3** (dashed line) in the listed solvents in the inset.

Table 4.4. Absorption band of **1** and **3** in the visible region in four solvents with varying dielectric constants and the corresponding ϵ value.

Solvent (dielectric constant)	1			
	λ	Absorbance	Concentration (μM)	ϵ
Pentane (2)	434	0.132	21.7	6100
THF (8)	428	0.107	20.3	5300
CH ₂ Cl ₂ (9)	431	0.128	19.5	6600
Ethanol (25)	431	0.099	35.5	2800
	3			
	λ	Absorbance	Concentration (μM)	ϵ
Pentane (2)	463	0.0297	36.6	811
THF (8)	463	0.0837	64.5	1300
CH ₂ Cl ₂ (9)	461	0.0278	65.7	423
Ethanol (25)	462	0.160	103.0	1560

Conclusions

The terthiophene analogue of **3** was characterized by ^1H NMR, IR spectroscopy, X-ray crystallography, and UV-visible absorption spectroscopy as described above. Changing the 3,4-thiophenedithiol for the 2,5-bis-2',2''-thiophen-2-yl-3,4-thiophenedithiol did not cause a considerable shift of the experimental $\nu\text{-CO}$ stretching frequencies, but a fourth peak was observed for **1** that is not present for **2** or **3**, as shown in Figure 4.1. This may be due to a perturbed geometry or multiple conformers of the complex in solution that removes the accidental degeneracy of the two stretching frequencies observed at 2008 and 2006 cm^{-1} . The removal of this accidental degeneracy separates the two IR absorption peaks by a sufficient amount of energy allowing the peaks to be resolved. Another difference between **1** and **3** was observed in the UV-visible absorption spectra in which it was found that **1** had a broad absorption in the visible region with a λ_{max} of 431 nm in CH_2Cl_2 with a larger extinction coefficient than **3**, regardless of the solvent. The extinction coefficient observed for **1** is also in the range of a charge-transfer band, and if this is a ligand-to-metal charge transfer, then **1** may be capable of being used as a potential photocatalyst for the production of H_2 .

Chapter 5 : ELECTROCHEMISTRY AND COMPUTATIONAL VALIDATIONS FOR (2,5-BIS-(2',2''-THIOPHEN-2-YL)-THIOPHENE- μ -3,4-DITHIOLATO)DIIRON HEXACARBONYL

Introduction

The precatalysts **2** and **3** have previously been reported for their individual electrocatalytic capabilities of producing H₂ from acetic acid in acetonitrile.^{32,53} The proposed catalytic mechanism for H₂ production by **3** was found to be analogous to **2**, and is shown in Figure 5.1, and is an (E)ECEC mechanism, where E represents an electrochemical process, and C represents a chemical step.^{32,53} After the first reduction of **3** to **3**¹⁻, step (E) which is required only once to activate the catalyst, a geometric rearrangement occurs that causes a lengthening of a Fe-S bond and a carbonyl ligand rotating into a bridging position between the two iron centers. Due to this rearrangement, the second reduction occurs at a potential less negative than the first, which is known as potential inversion, and the experimental reduction of this two electron reduction is observed at -1.33 V vs Fc⁺/Fc. Following the reduction, the complex is then protonated by acetic acid to form the anion, **3H**⁻, which then undergoes a second reduction at -1.90 V to form **3H**²⁻. At this state, **3H**²⁻ is capable of H₂ evolution as it is hydridic enough for a second protonation by acetic acid to occur. The reduction peak at -1.90 V, measured at the half-peak potential, was shown to be the catalytic peak as the maximum current increased at this potential with higher concentrations of acetic acid. The half-peak potential is defined as the voltage corresponding to half of the maximum current at the onset of a cathodic or anodic peak for an irreversible process.⁷⁶ Using DFT methods, the evolution of H₂ at this condition was determined to be spontaneous with a Gibb's free energy value of the catalytic H₂ production step being -35 kcal/mole. Although **3** catalytically produced H₂ using acetic acid, an overpotential for catalysis of -0.44 V was observed, and the catalytic current was lower compared to **2**.^{32,53} A qualitative determination for catalytic efficiency using electrochemical

analysis was described by Evans et al. as the ratio of the catalytic current (i_{cat}) and the catalyst reduction current (i_d) with no acid present, divided by the ratio of the concentration of the acid (C_{HA}) and the concentration of the catalyst (C_{cat}). For the efficiency of a catalyst, Evans assigned a catalyst as being either strong (S) for $C.E. > 0.75$, medium (M) for $0.25 < C.E. < 0.75$, or weak (W) $C.E. < 0.25$. Using Evan's method, **2** and **3** have been described as having a medium catalytic efficiency in the presence of acetic acid.^{17,32,53}

$$C.E. = \frac{i_{cat}/i_d}{C_{HA}/C_{cat}}$$

Tilley and coworkers recently showed that the dianion of **2** has the rotated geometry structure with the broken Fe-S bond and the bridging carbonyl ligand. Tilley et al. accomplished this by reducing **2** with sodium metal in tetrahydrofuran, and obtained an X-ray crystallographic structure of the product that showed **2**²⁻ had crystallized as a dimer with the rotated geometry.⁷⁷ The protonated **2H**⁻ complex was also generated by using benzoic acid, and ¹H NMR spectroscopic data along with DFT calculations supported formation of the bridging μ -hydride complex that had previously been suggested as the favorable location for protonation of the dianion.^{53,77} From **2** and **3**, it was hypothesized that **1** would also be capable of generating molecular hydrogen under similar conditions, as **1** is an extension of the conjugated thiophene system from the monothiophene to the terthiophene. In this work, it was found that **1** was a procatalyst for the reduction of protons to H₂ electrochemically in dichloromethane (CH₂Cl₂). Acetonitrile was tested, however reproducible results were not obtained preventing direct comparisons of **1** from being made to **2** and **3**. In CH₂Cl₂, a more positive potential was observed for **1** at the catalytic peak compared to both **2** and **3** (Figure 5.4), indicating that **1** reduces protons to H₂ at a lower potential. However, an

overpotential cannot be determined as the standard potential of acetic acid is not known in CH_2Cl_2 .¹⁷

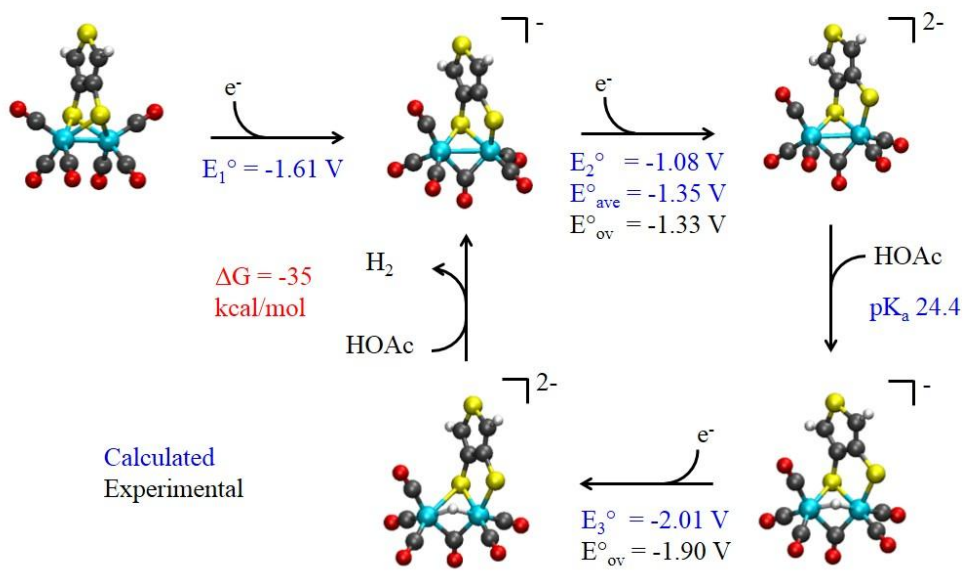


Figure 5.1. Catalytic mechanism for **3** in acetonitrile with the calculated (blue) and experimental (black) values for the reduction potentials.

Results and Discussion

Electrochemical Investigations

Electrochemical analysis for the reduction potential of **1** was performed in acetonitrile as well as in dichloromethane (CH_2Cl_2). However, reproducible results of the electrochemical analysis were not obtained for **1** in acetonitrile. Decomposition of the catalyst was observed based on a color change of the solution from orange to a deep red over time. This decomposed material caused a change in the reduction scans as new cathodic peaks appeared that weren't present in the initial reduction scans. The glassy carbon electrode was polished between scans to remove a deposited material, however the unknown cathodic peaks were still present in the reduction scans, and reproducible scans were not obtained. After switching to CH_2Cl_2 , reproducible results of **1** were obtained by polishing the working electrode between scans, and compared to the cyclic voltammograms (CV) of **2** and **3** in the same solvent. Due to the reproducibility in the scans, all electrochemical analysis is reported in CH_2Cl_2 . The cyclic voltammogram of **1** at a 0.10 V/s scan rate, shown in Figure 5.2, displays a reversible reduction centered at -1.39 V vs Fc^+/Fc . The half-wave reduction potentials of **2** and **3**, indicated by the red and green dashed lines, are 0.05 V and 0.08 V more negative under the same conditions. The observed reduction for **2** matches the previously reported reduction potential in CH_2Cl_2 .³¹ After this reduction, no additional cathodic peaks were observed for either catalyst before the onset of the direct reduction of CH_2Cl_2 at -2.37 V.

The 0.05 V/s to 10.0 V/s scan rate study of **1** and **2** in CH_2Cl_2 is shown in Figure 5.3 below. The reduction for **1** in CH_2Cl_2 is assigned as a two-electron potentially inverted process. The number of electrons involved in the first reduction were determined by comparison of maximum current to the maximum current of **2**, which is a known two electron reduction.⁵³ Furthermore, the

reduction of **1** at -1.39 V is approximately twice as large as the known one electron oxidation of ferrocene under the same conditions. Scan rate studies of **1** show that the maximum normalized current begins to decrease at scan rates greater than 0.10 V/s. Potential inversion is observed due to a geometric rearrangement in which **1** rotates from the all terminal CO complex to one with a bridging CO between the iron centers, and a lengthening of one of the Fe-S bonds, as is observed with similar hydrogenase mimics.^{32,53} The HOMO and LUMO plots of **1**, **2**, and **3** are shown in Figure 5.4 below. As can be seen from the LUMO plots, the orbital character is primarily anti-bonding between the iron and sulfur atoms for all three complexes. The addition of an electron to this orbital will cause a destabilization of the Fe-S bond, causing a lengthening of that bond, initiating the formation of a rotated structure which was demonstrated experimentally by Tilley and coworkers for **2**.⁷⁷ At scan rates faster than 0.10 V/s, the decrease in the maximum normalized current is an indication that the kinetics of the geometric rearrangement is being outpaced by the scan rate, altering the two electron potential inverse process to a one electron process.^{32,53}

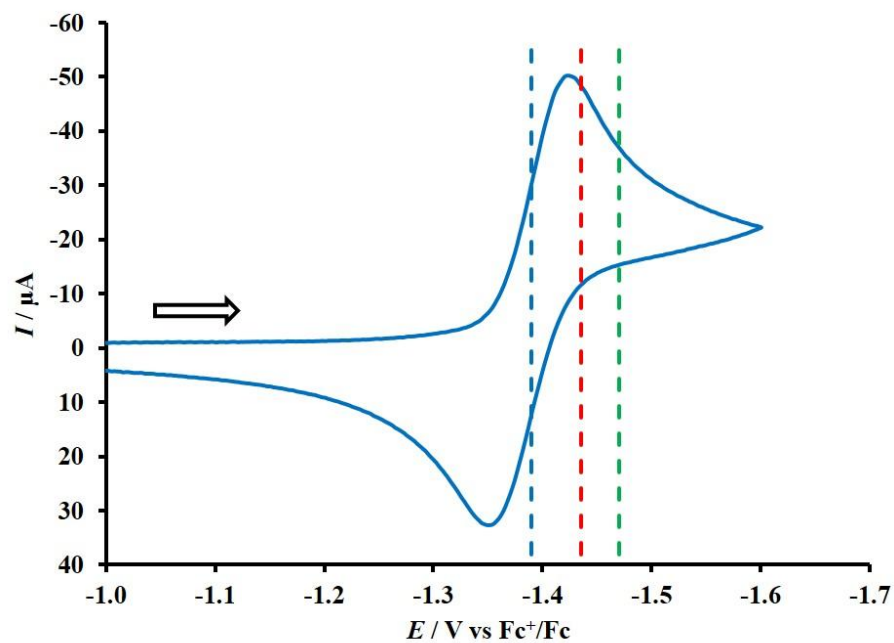


Figure 5.25. Cyclic voltammogram of **1** in dichloromethane with 0.2 M tetra-*n*-butylammonium hexafluorophosphate on a 0.3 cm diameter glassy carbon working electrode at a scan rate of 0.100 V/s under an argon atmosphere. The black arrow indicates the direction of the initial scan. The dashed lines indicate the half-wave potential for ca. 1 mM **1** (blue), 1 mM **2** (red), and 0.5 mM **3** (green).

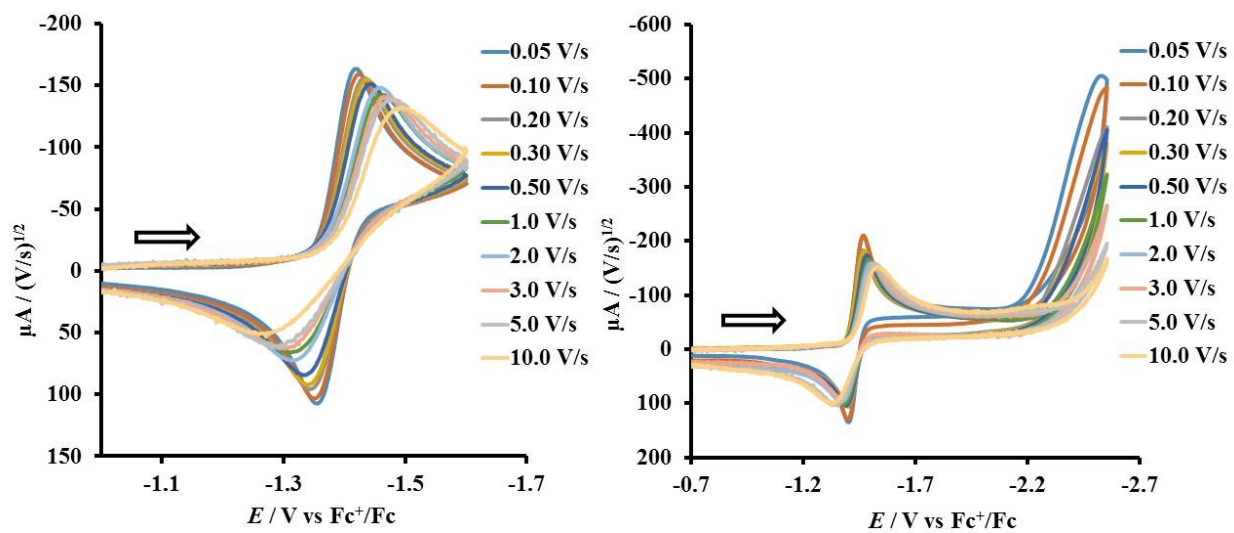


Figure 5.3. Cyclic voltammograms of 1 mM **1** (left) and **2** (right) collected in CH_2Cl_2 with 0.2 M tetra-*n*-butylammonium hexafluorophosphate on a 0.3 cm diameter glassy carbon working electrode. Scan rates are listed for each complex.

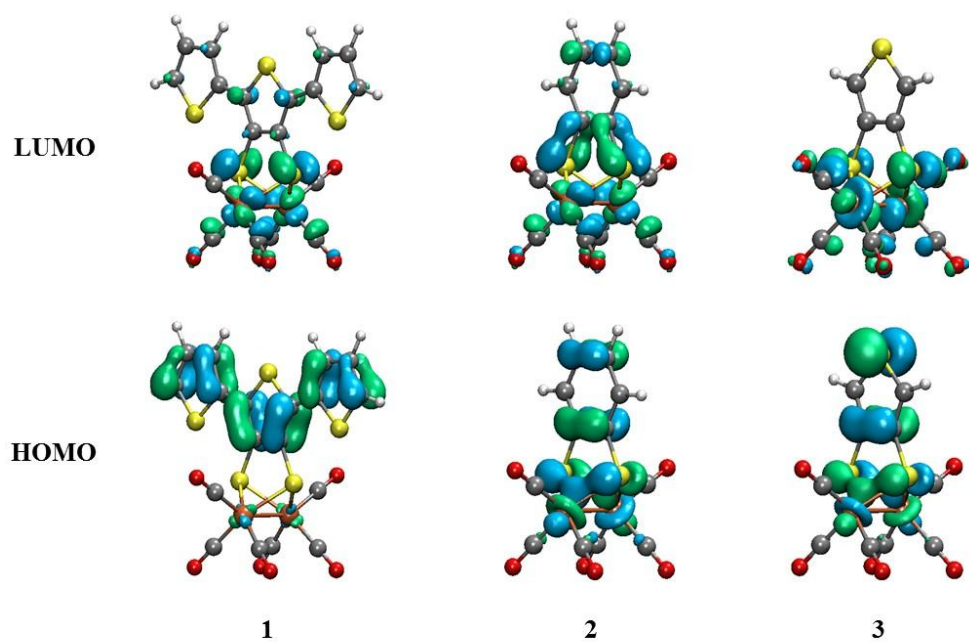


Figure 5.4. Comparison of the HOMO (bottom) and LUMO (top) plots of **1** (left), **2** (middle) and **3** (right).

Catalysis

The catalytic activity for **1** in CH_2Cl_2 in the presence of 2-50 mM acetic acid was explored by cyclic voltammetry, and is shown in Figure 5.5. **2** and **3** were analyzed under the same conditions for comparison to **1**. Upon the first addition of acetic acid, the initial reduction potential of **1** shifted anodically by approximately 0.04 V. A small increase in the current was also observed with the addition of acid, but the current did not continue to increase with higher concentrations of acid indicating that catalysis is not occurring at this potential. Scanning to more negative potentials with acetic acid present, a new cathodic peak was observed at -1.82 V vs Fc^+/Fc . The maximum current of this peak increased with each addition of acetic acid, corresponding to a catalytic reduction of protons to molecular hydrogen.^{32,53} The CV for the 50 mM acetic acid scan for the three catalysts' is shown in Figure 5.6. The initial reduction potential of all three complexes follows the same trend as was observed in Figure 5.2, including the anodic 0.04 V shift of the first reduction peak in the presence of acetic acid.

The half-peak potential for the catalytic peak for **1**, **2**, and **3** were assigned at -1.82 V, -1.96 V, and -1.98 V, respectively. From Figure 5.6, it is seen that **1** electrochemically produces H_2 at a more positive potential vs Fc^+/Fc in CH_2Cl_2 than either **2** or **3**, but has the lowest maximum current observed at the 50 mM acetic acid concentration scan, indicating that **1** is catalytically less efficient using Evans' method.¹⁷ Another means of determining the effectiveness of these catalysts is by evaluating the overpotential for catalysis. The overpotential for catalysis is described as the difference between the potential at which catalysis is observed for H_2 production and the standard potential of the reduction of the acid, in this case acetic acid.¹⁷ In acetonitrile, the standard potential for reduction of acetic acid is -1.46 V vs Fc^+/Fc ,⁷⁸ however as previously stated, the standard potential for acetic acid in CH_2Cl_2 is not known, so therefore an exact value for the overpotential

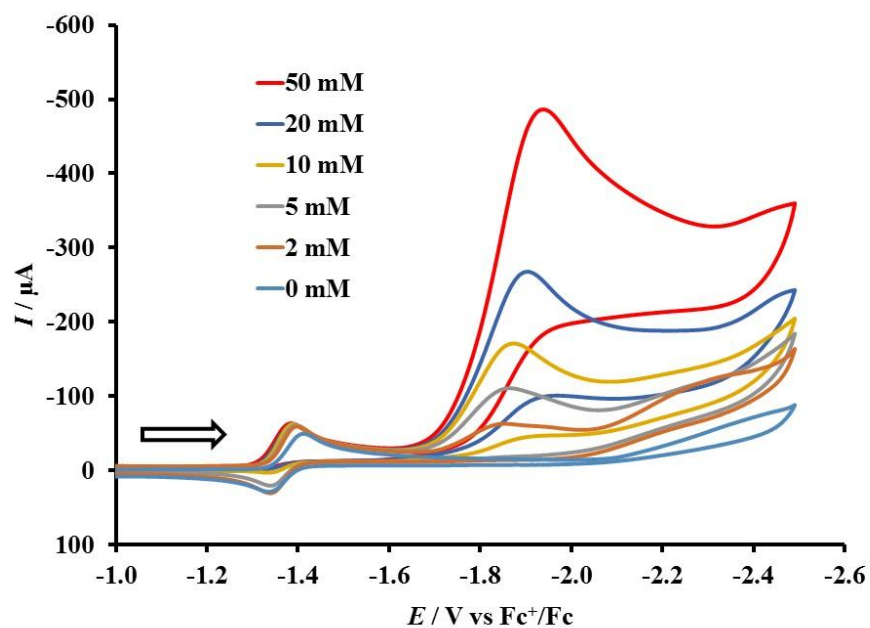


Figure 5.55. Cyclic voltammogram of ca. 1 mM **1** in the presence of various acetic acid concentrations with 0.2 M tetra-*n*-butylammonium hexafluorophosphate in CH₂Cl₂ on a glassy carbon working electrode at a 0.10 V/s scan rate under an Ar atmosphere. The black arrow indicates the direction of the initial scan.

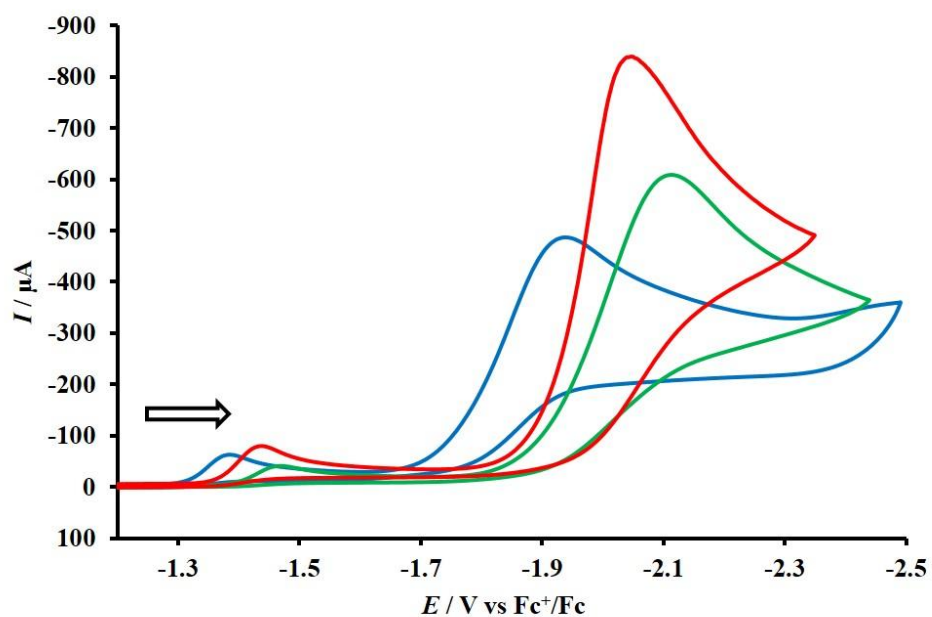


Figure 5.6. Voltammogram of ca. 1 mM **1** (blue) and **2** (red), and ca. 0.5 mM **3** (green) in the presence of 50 mM acetic acid at 0.10 V/s with 0.2 M tetra-*n*-butylammonium hexafluorophosphate in CH_2Cl_2 . The black arrow indicates the initial scan direction.

of these catalysts cannot be determined. Even though an overpotential cannot be determined, Figure 5.6 shows that **1** has the most positive catalytic potential at -1.82 V, 0.14 and 0.16 V more positive than **2** and **3**, respectively.

Comparison of Computations to Experimental Observed Values

Validation for the computational methods is based on the capability of the calculations to accurately account for the experimentally observed molecular geometry from X-ray crystallography and the ν -CO stretching frequencies. Through validation of the calculations, predictions can be made for the reduction potentials for intermediate species in the catalytic mechanism for the production of H₂. Selected bond lengths and angles from the computational gas-phase calculation for **1** are compared to the experimental X-ray crystallographic structure for **1** in Table 5.1. The table shows that the structural parameters of the DFT and X-ray crystal structure are in good agreement as the bond lengths and angles match within hundredths of an angstrom and three degrees, indicating that the computations are modeling the geometric properties well, with the exception of one of the torsion angles in the thiophene rings.

Additional validation for the DFT calculations was done via comparison of the computed carbonyl stretching frequencies with that of the experimental IR spectrum of **1** (Figure 5.7). As previously mentioned, the carbonyl stretching frequencies are sensitive to electron density at the metal center. An electron rich metal will have a stronger π -backbonding interaction than that of an electron deficient metal with the carbonyl ligand, causing a decrease in energy for the stretching frequencies. Figure 5.7 shows that there is good agreement between the calculated carbonyl stretching frequencies and the experimental values. The predicted stretching frequencies were scaled by a factor of 0.38% to account for the differences between gas-phase calculations and the experimental IRs taken in hexanes solutions. This small scaling factor and the correct number of

Table 5.1. Comparison of the DFT geometry optimized structure to the X-ray crystallographic data for **1**.^a

Bond/Angle ^b	X-ray ^c	DFT ^d
Fe-Fe	2.4889(7)	2.437
S•••S	2.980(1)	2.993
S-C _L	1.766(3)	1.771
Fe-S	2.2766(8)	2.294
Fe-C _a	1.811(3)	1.785
Fe-C _b	1.798(3)	1.778
C _a -O _a	1.135(4)	1.155
C _b -O _b	1.143(4)	1.157
Fe-S-Fe	66.28(2)	65.53
C _a -Fe-C _b	99.7(1)	99.47
C _b -Fe-C _b	90.3(1)	91.23
C _a -Fe-Fe	147.7(1)	150.47
C _b -Fe-Fe	103.0(1)	101.06
S-Fe-S	81.76(3)	81.45
S4-C14-C15-S5	176.0(2)	179.99
S4-C11-C10-S3	-171.9(2)	-179.97

^aBond lengths are in Å; angles and torsion angles are in degrees. ^bC_a refers to the apical CO in the local square-based pyramid geometry of each Fe, and C_b refers to the basal CO. C_L refers to the carbon atom attached to the bridging sulfur atom. ^cNumbers in parentheses denote error in the measurement of the last decimal place. ^dSee experimental chapter for the details on the DFT methods.

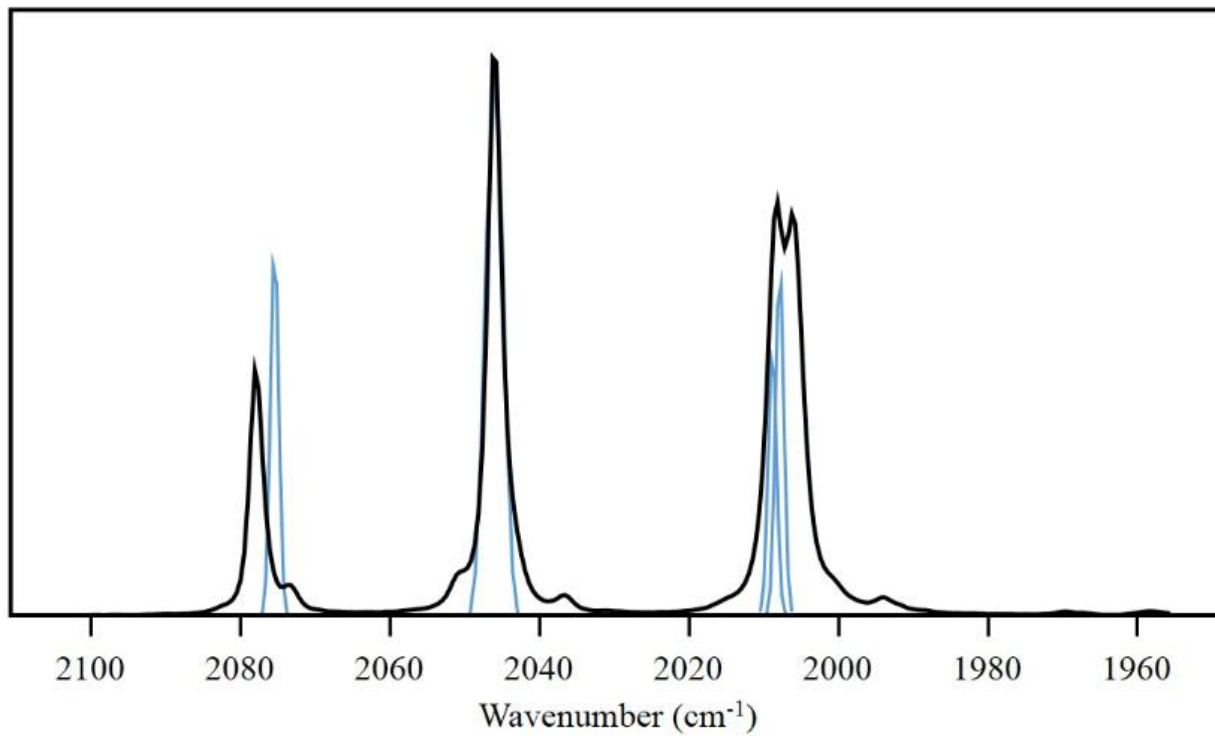


Figure 5.75. Experimental (black) and calculated (blue) carbonyl stretching frequencies of **1**. The experimental frequencies were collected in hexanes using an air-free IR cell.

frequencies predicted indicates that the electronic structure and geometry for **1** is being adequately modeled by the computational methods.

Using DFT methods, previously described in the Experimental chapter, a catalytic mechanism was proposed for **1** that involves reduction of protons via an ECEC mechanism at the Fe-Fe center, shown in Figure 5.8, similar to the mechanisms reported for **2** and **3**.^{32,53} The computational solvation effects were calculated in acetonitrile since the reduction potentials are not modeled well in solvents with low dielectric constants such as CH₂Cl₂ ($\epsilon = 9$) due to an ion-pairing stabilization effect in solution.^{79,80} The first reduction potential for **1** was calculated to be at -1.58 V, and the second reduction potential was calculated to be -1.03 V, indicating that the calculations are predicting the observed potential inversion. The average of these two calculated potentials is -1.31 V, which is 0.08 V more positive than the experimental value observed at -1.39 V. Once **1** has been reduced to the dianion, **1**²⁻, a geometric rearrangement occurs to the rotated structure in which an Fe-S bond breaks and a carbonyl moves into a bridging position, as shown in Figure 5.8. As the dianion, **1**²⁻ should be basic enough to be protonated by acetic acid, with the computations predicting that a μ -hydride is formed across the Fe centers as the more thermodynamically favored species. On the return oxidation scan in Figure 5.5, the reversible oxidation of **1**²⁻ to **1** at -1.39 V became irreversible after the 5 mM addition of acetic acid, and a new anodic peak at a less negative potential, which is attributed to the oxidation of the anion **1H**⁻ to **1H**, similar to what was observed and reported for **2**.⁵³

A catalytic peak was not observed at -1.39 V indicating that the hydride species, **1H**⁻, is not hydridic enough to react with another molecule of acetic acid, therefore a third electron is needed to continue the catalytic mechanism. The third reduction is calculated to occur at -2.06 V, which is 0.24 V more negative than the experimentally observed value. This difference is most

likely due to an ion pairing stabilization effect in solution of the singly protonated dianion complex, $\mathbf{1H}^{2-}$, by the tetra-*n*-butylammonium cation, which the computations are not modeling. Ion-pairing has been shown to stabilize oxidized compounds in solution, which would imply that reduced compounds may also be stabilized by the electrolyte.⁸¹ Following the third reduction, $\mathbf{1H}^{2-}$ undergoes another protonation by acetic acid and spontaneously evolves molecular hydrogen, based on the increasing catalytic current seen in Figure 5.4, and the calculated Gibb's free energy of the reaction being -13 kcal/mole. Once molecular hydrogen has been evolved, the anion of $\mathbf{1}^-$ enters back into the catalytic cycle.

Conclusions

The terthiophene analogue of **3** was successfully studied electrochemically in CH_2Cl_2 . The DFT computational data was also validated via comparison to the X-ray crystallographic data and infrared CO stretching frequencies. With the validation of the DFT methods, a catalytic mechanism was proposed for **1** by determining the most thermodynamically favored structure at each step. This mechanism was found to be similar to that of **2** and **3** with a potential inverse process occurring at the first reduction and a μ -hydride being formed upon protonation of $\mathbf{1}^{2-}$. However, the anion, $\mathbf{1}^-$, was not found to have the rotated geometry after the first reduction as was suggested for **2** and **3**, but remained in the non-rotated geometry for the thermodynamically favored structure. The potential for the catalytic peak was calculated to be -2.06 V vs Fc^+/Fc in acetonitrile, and is very similar to the calculated potentials for **2** (-2.05 V)⁵³ and **3** (-2.01 V).³² However, the experimental catalytic peak that was observed in CH_2Cl_2 is 0.24 V more positive than was predicted by the calculations, and was 0.14 V and 0.16 V more positive than **2** and **3**, respectively. From the IR comparison of all three catalysts in Figure 4.2, there is very little difference between the electronic density at the 2Fe2S center of these complexes, yet **1** is reduced and catalytically

produces H₂ at lower potentials. This positive shift observed in the reduction potentials is most likely attributed to a more stabilized product in the anion, **1**⁻, after evolution of hydrogen from **1H**²⁻ and acetic acid. The anion complex of **1**⁻ may be able to delocalize the negative charge into the conjugated terthiophene system, unlike **2**⁻ and **3**⁻. Along with the positive shift in the reduction potentials, **1** successfully produced molecular hydrogen electrochemically in the presence of acetic acid.

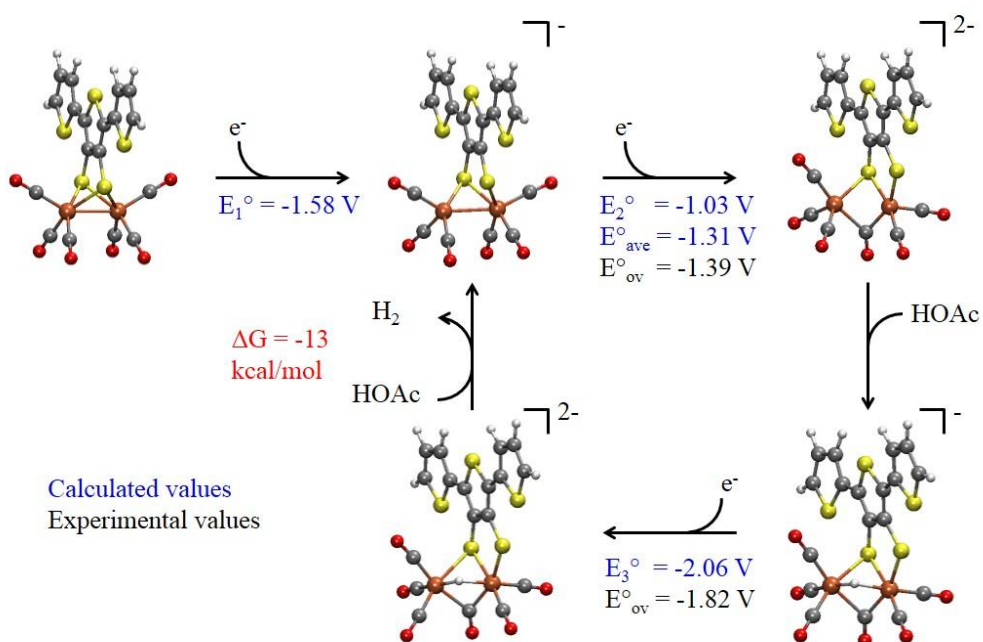


Figure 5.8. Proposed catalytic mechanism for **1** for the reduction of protons to H_2 .

Chapter 6 : CONCLUSIONS AND FUTURE DIRECTIONS

The [FeFe]-hydrogenase mimic, **1**, was successfully synthesized and investigated via ^1H NMR, IR spectroscopy, UV-visible absorption spectroscopy, X-ray crystallography, and electrochemistry. Density functional theory calculations were used to determine a catalytic mechanism for the production of molecular hydrogen by the mimic complex **1** and acetic acid. The DFT methods were validated by comparison of the predicted geometric and electronic properties to the experimental values.

Effect of the 2,5-bis-(2',2''-thiophen-2-yl)-thiophene- μ -3,4-dithiolato ligand

With the 2,5-bis-(2',2''-thiophen-2-yl)-thiophene- μ -3,4-dithiolato ligand used in place of either the 1,2-benzenedithiolato or 3,4-thiophenedithiolato ligand, a very similar geometric and electronic structure was observed compared to the other two catalysts. This was shown in the X-ray crystallographic data as the atom bond lengths and angles were all very similar between each catalyst. The infrared spectroscopy of **1** compared to **2** and **3** showed that there was a negligible shift of the ν -CO stretching frequencies for each peak by approximately only 2 cm^{-1} . A noticeable difference observed in the IR spectroscopy was the separation of the accidental degeneracy of the stretching frequency peak observed at 2008 and 2006 cm^{-1} for **1**, while only one peak is observed for **2** and **3** in the same region. Although the geometric and electronic properties were similar between the three catalysts, when studied electrochemically in CH_2Cl_2 , **1** was observed to have a potentially inverted reversible two electron reduction peak at -1.39 V vs Fc^+/Fc , and was 0.05 V and 0.08 V more positive than the reductions observed for **2** and **3**. This positive shift in the reduction potential suggests that the potentially inverted reduction of **1** to the dianion is more favorable than is the reduction of **2** and **3** even though the electronic properties are similar between the three catalysts. This observation may be due to the aryl dithiolate bridgehead of **1** providing

stability to the reduced catalyst by lowering the overall negative charge through the longer extended conjugation of the terthiophene system that is not available in the benzene and thiophene analogues. In addition to a lower potential for the initial reduction, **1** also catalytically produces molecular hydrogen from acetic acid at a lower potential compared to **2** and **3** by 0.14 V and 0.16 V vs Fc^+/Fc . However, the standard potential of acetic acid is not currently known in CH_2Cl_2 , and an overpotential of these catalysts in this solvent cannot be determined. Using DFT calculations, a catalytic mechanism was proposed for **1** and was similar, with the exception of the non-rotated geometry of the anion **1**⁻, to the proposed mechanisms of **2** and **3** for producing H_2 through an (E)ECEC mechanism. After the two electron potentially inverted reduction, the catalyst undergoes a geometric rearrangement where a Fe-S bond breaks and a carbonyl moves into a bridging position between the two Fe atoms. The breaking of the Fe-S bond is due to the repulsive interaction between the Fe and S as the reduction takes place in an anti-bonding orbital with respect to the Fe-S bond. With the addition of an electron to this orbital, the Fe and S atoms are pushed further apart, allowing the second reduction to occur at a lower potential than the first reduction, and the potentially inverted process is observed.

From the UV-visible absorption spectroscopy, **1** was found to have a broad absorption band in the visible region from about 400-500 nm with a molar extinction coefficient of $6500 (\text{M cm})^{-1}$ in CH_2Cl_2 , whereas **2** and **3** do not have any absorption bands in the same region. Based on the molar extinction coefficient, this indicates that there is charge transfer band present, and it most likely a ligand-to-metal charge transfer as the value is below that observed for a ligand-to-ligand π - π^* transition. This observed absorption band is promising for the use of **1** as an artificial photocatalytic mimic for the production of H_2 .

Future Directions

From the electrochemical data and DFT methods, the [FeFe]-hydrogenase mimic **1** was shown to be capable of producing H₂ using acetic acid in CH₂Cl₂. However, the CH₂Cl₂ solvent had to be used instead of CH₃CN due to a stability issue of the complex during the cyclic voltammetry experiment. The conditions of the degradation for the catalyst are not known, but from the electrochemistry as well as preliminary ¹H NMR experiments of the complex after it was stored at non-inert conditions and exposed to light, there was an observed decomposition of **1**. To improve the stability of this catalyst, the decomposition pathway should be determined so that **1** can be modified so as to prevent or minimize the deactivation of the catalyst. To do this, the decomposed material could be obtained using two different methods. The first would be to isolate the decomposed material that was removed using a silica plug to purify the sample for ¹H NMR spectroscopy. The second method would use sublimation to separate the pure catalyst from the decomposed material. Once isolated, IR spectroscopy will be used to analyze the ν-CO stretching frequencies to determine how it differs from **1**. If a single crystal of the decomposed material can be obtained, X-ray crystallography will be used to determine the structure of the decomposed product. If neither of these techniques work, the pure compound, **1**, can be dissolved in hexanes and added to an air free IR cell and the decomposition can be monitored over time to observe how the carbonyl stretching frequencies change. Lastly, as **1** was designed for purpose of being used as a photocatalyst for H₂ production, therefore it will need to be tested to determine if molecular hydrogen can be generated. To do this experiment, a Xenon Arc lamp with a 400 nm filter to remove the ultra-violet radiation will be used to photo-excite the catalyst in the presence of acetic acid and the electron donor triethyl amine. Gas chromatography will be used to determine the

amount of H₂ produced and the TON for the catalyst, as is done for similar photosynthetic catalysts.⁸²

REFERENCES:

- (1) Lewis, N. S. *Powering the Planet*. <http://calteches.library.caltech.edu/4259/> (accessed November 6, 2013).
- (2) Evans, D. J.; Pickett, C. J. *Chem. Soc. Rev.* **2003**, *32*, 268.
- (3) Tard, C.; Pickett, C. J. *Chem. Rev.* **2009**, *109*, 2245.
- (4) Anonymous How Fuel Cells Work. https://www.fueleconomy.gov/feg/fcv_PEM.shtml (accessed January 24, 2014).
- (5) T-Raissi, A. Technoeconomic Analysis of Area II Hydrogen Production - Part 1. <http://www1.eere.energy.gov/hydrogenandfuelcells/pdfs/30535bq.pdf> (accessed January 24, 2014).
- (6) Sasaki, K.; Naohara, H.; Cai, Y.; Choi, Y. M.; Liu, P.; Vukmirovic, M. B.; Wang, J. X.; Adzic, R. R. *Angew. Chem. Int. Ed.* **2010**, *49*, 8602.
- (7) Peters, J. W. *Science* **1999**, *283*, 2102.
- (8) Nicolet, Y.; Piras, C.; Legrand, P.; Hatchikian, C.; Fontecilla-Camps, J. C. *Struct. Fold Des.* **1999**, *7*, 13.
- (9) Frey, M. *ChemBioChem* **2002**, *3*, 153.
- (10) Stephenson, M.; Stickland, L. H. *Biochem. J.* **1931**, *25*, 215.
- (11) Sadana, J. C.; Rittenberg, D. *Proc. Natl. Acad. Sci. U. S. A.* **1963**, *50*, 900.
- (12) Buchanan, B. B.; Lovenberg, W.; Rabinowitz, J. C. *Proc. Natl. Acad. Sci. U. S. A.* **1963**, *49*, 345.
- (13) Lovenberg, W.; Buchanan, B. B.; Rabinowitz, J. C. *J. Biol. Chem.* **1963**, *238*, 3899.
- (14) Nakos, G.; Mortenson, L. E. *Biochemistry (N. Y.)* **1971**, *10*, 2442.
- (15) Nakos, G.; Mortenson, L. *Biochim. Biophys. Acta* **1971**, *227*, 576.
- (16) Albracht, S. P. J.; Graf, E. G.; Thauer, R. K. *FEBS Lett.* **1982**, *140*, 311.
- (17) Felton, G. A. N.; Mebi, C. A.; Petro, B. J.; Vannucci, A. K.; Evans, D. H.; Glass, R. S.; Lichtenberger, D. L. *J. Organomet. Chem.* **2009**, *694*, 2681.
- (18) Tard, C.; Pickett, C. J. *Chem. Rev.* **2009**, *109*, 2245.

- (19) Nicolet, Y.; Lemon, B. J.; Fontecilla-Camps, J. C.; Peters, J. W. *Trends Biochem. Sci.* **2000**, *25*, 138.
- (20) Pilet, E.; Nicolet, Y.; Mathevon, C.; Douki, T.; Fontecilla-Camps, J. C.; Fontecave, M. *FEBS Lett.* **2009**, *538* (3), 506.
- (21) Wei, C. H.; Dahl, L. F. *Inorg. Chem.* **1965**, *4*, 1.
- (22) Lyon, E. J.; Georgakaki, I. P.; Rabenspies, J. H.; Darensbourg, M. Y. *Angew. Chem. Int. Ed.* **1999**, *38*, 3178.
- (23) Mejia-Rodriguez, R.; Chong, D.; Reibenspies, J. H.; Soriaga, M. P.; Darensbourg, M. Y. *J. Am. Chem. Soc.* **2004**, *126*, 12004.
- (24) Borg, S. J.; Behrsing, T.; Best, S. P.; Razavet, M.; Liu, X.; Pickett, C. J. *J. Am. Chem. Soc.* **2004**, *126*, 16988.
- (25) Joshi, H. K.; Inscore, F. E.; Schirlin, J. T.; Dhawan, I. K.; Carducci, M. D.; Bill, T. G.; Enemark, J. H. *Inorg. Chim. Acta* **2002**, *337*, 275.
- (26) Cooney, J. J.; Cranswick, M. A.; Gruhn, N. E.; Joshi, H. K.; Enemark, J. H. *Inorg. Chem.* **2004**, *43*, 8110.
- (27) Joshi, H. K.; Enemark, J. H. *J. Am. Chem. Soc.* **2004**, *126*, 11784.
- (28) Joshi, H. K.; Cooney, J. J. A.; Inscore, F. E.; Gruhn, N. E.; Lichtenberger, D. L.; Enemark, J. H. *Proc. Natl. Acad. Sci. U. S. A.* **2003**, *100*, 3719.
- (29) Joshi, H. K.; Inscore, F. E.; Schirlin, J. T.; Dhawan, I. K.; Carducci, M. D.; Bill, T. G.; Enemark, J. H. *Inorg. Chim. Acta* **2002**, *337*, 275.
- (30) Felton, G. A. N.; Vannucci, A. K.; Chen, J.; Lockett, L. T.; Okumura, N.; Petro, B. J.; Zakai, U. I.; Evans, D. H.; Glass, R. S.; Lichtenberger, D. L. *J. Am. Chem. Soc.* **2007**, *129*, 12521.
- (31) Capon, J. F.; Gloaguen, F.; Schollhammer, P.; Talarmin, J. *J. Electroanal. Chem.* **2004**, *566*, 241.
- (32) Stratton, L. M. Preparation and Characterization of [FeFe]Hydrogenase Active Site Mimics Studied by Gas-Phase Photoelectron Spectroscopy, Electrochemistry, and Computational Models, The University of Arizona, 2012.
- (33) Barber, J. *Chem. Soc. Rev.* **2009**, *38*, 185.
- (34) Wang, F.; Wang, W.; Wang, H.; Si, G.; Tung, C.; Wu, L. *ACS Catal.* **2012**, *2*, 407.

- (35) Cui, H.; Hu, M.; Wen, H.; Chai, G.; Ma, C.; Chen, H.; Chen, C. *Dalton Trans.* **2012**, *41*, 13899.
- (36) Wang, M.; Chen, L.; Li, X.; Sun, L. *Dalton Trans.* **2011**, *40*, 12793.
- (37) Samuel, A. P. S.; Co, D. T.; Stern, C. L.; Wasielewski, M. R. *J. Am. Chem. Soc.* **2010**, *132*, 8813.
- (38) Wolpher, H.; Borgström, M.; Hammarström, L.; Bergquist, J.; Sundström, V.; Styring, S.; Sun, L.; Åkermark, B. *Inorg. Chem. Commun.* **2003**, *6*, 989.
- (39) Ott, S.; Borgström, M.; Kritikos, M.; Lomoth, R.; Bergquist, J.; Åkermark, B.; Hammarström, L.; Sun, L. *Inorg. Chem.* **2004**, *43*, 4683.
- (40) Ekstrom, J.; Abrahamsson, M.; Olson, C.; Bergquist, J.; Kaynak, F. B.; Eriksson, L.; Sun, L.; Becker, H.; Åkermark, B.; Hammarström, L.; Ott, S. *Dalton Trans.* **2006**, , 4599.
- (41) Song, L.; Tang, M.; Mei, S.; Huang, J.; Hu, Q. *Organometallics* **2007**, *26*, 1575.
- (42) Li, X.; Wang, M.; Zhang, S.; Pan, J.; Na, Y.; Liu, J.; Åkermark, B.; Sun, L. *J. Phys. Chem. B* **2008**, *112*, 8198.
- (43) Kluwer, A. M.; Kapre, R.; Hartl, F.; Lutz, M.; Spek, A. L.; Brouwer, A. M.; van Leeuwen, P. W. N. M.; Reek, J. N. H. *Proc. Natl. Acad. Sci. U S A* **2009**, *106*, 10460.
- (44) Song, L.; Tang, M.; Su, F.; Hu, Q. *Angew. Chem. Int. Ed.* **2006**, *45*, 1130.
- (45) Wang, W.; Wang, F.; Wang, H.; Si, G.; Tung, C.; Wu, L. *Chem. Asian J.* **2010**, *5*, 1796.
- (46) Zhang, P.; Wang, M.; Na, Y.; Li, X.; Jiang, Y.; Sun, L. *Dalton Trans.* **2010**, *39*, 1204.
- (47) Streich, D.; Astuti, Y.; Orlandi, M.; Schwartz, L.; Lomoth, R.; Hammarström, L.; Ott, S. *Chem. - Eur. J.* **2010**, *16*, 60.
- (48) Wang, F.; Wang, W.; Wang, X.; Wang, H.; Tung, C.; Wu, L. *Angew. Chem. Int. Ed.* **2011**, *50*, 3193.
- (49) Zhang, F.; Wu, D.; Xu, Y.; Feng, X. *J. Mater. Chem.* **2011**, *21*, 17590.
- (50) Sease, J. W.; Zechmeister, L. *J. Am. Chem. Soc.* **1947**, *69*, 270.
- (51) Mason, C. R.; Li, Y.; O'Brien, P.; Findlay, N. J.; Skabara, P. J. *Beilstein J. Org. Chem.* **2011**, *7*, 1722.
- (52) Carpino, L. A. *J. Org. Chem.* **1970**, *35*, 3971.

- (53) Felton, G. A. N.; Vannucci, A. K.; Chen, J.; Lockett, L. T.; Okumura, N.; Petro, B. J.; Zakai, U. I.; Evans, D. H.; Glass, R. S.; Lichtenberger, D. L. *J. Am. Chem. Soc.* **2007**, *129*, 12521.
- (54) ADF2012.01b, SCM, Theoretical Chemistry, Vrije Universiteit, Amsterdam, The Netherlands, **2012**, <http://www.scm.com>.
- (55) Guerra, C. F.; Snijders, J. G.; Te Velde, G.; Baerends, E. J. *Theor. Chem. Acc.* **1998**, *99*, 391.
- (56) Te Velde, G.; Bickelhaupt, F. M.; Baerends, E. J.; Fonseca Guerra, C.; Van Gisbergen, S. J. A.; Snijders, J. G.; Ziegler, T. *J. Comput. Chem.* **2001**, *22*, 931.
- (57) Stoll, H.; Pavlidou, C. M. E.; Preuss, H. *Theor. Chim. Acta* **1978**, *49*, 143.
- (58) Zhang, Y.; Wu, A.; Xu, X.; Yan, Y. *Chem. Phys. Lett.* **2006**, *421*, 383.
- (59) Swart, M.; Ehlers, A. W.; Lammertsma, K. *Mol. Phys.* **2004**, *102*, 2467.
- (60) van Lenthe, E.; Ehlers, A.; Baerends, E. *J. Chem. Phys.* **1999**, *110*, 8943.
- (61) Klamt, A. *J. Phys. Chem.* **1995**, *99*, 2224.
- (62) Jensen, F. *Introduction to Computational Chemistry*; Wiley: Chichester, England, 2002.
- (63) Dolomanov, O. V.; Bourhis, L. J.; Gildea, R. J.; Howard, J. A. K.; Puschmann, H. *J. Appl. Crystallogr.* **2009**, *42*, 339.
- (64) Sheldrick, G. M. *Acta Crystallographica Section A* **2008**, *64*, 112.
- (65) Cabeza, J. A.; Martinez-Garcia, M. A.; Riera, V.; Ardura, D.; Garcia-Granda, S. *Organometallics* **1998**, *17*, 1471.
- (66) Schwartz, L.; Singh, P. S.; Eriksson, L.; Lomoth, R.; Ott, S. *Comp. Rend. Chim.* **2008**, *11*, 875.
- (67) Chen, J.; Vannucci, A. K.; Mebi, C. A.; Okumura, N.; Borowski, S. C.; Swenson, M.; Lockett, L. T.; Evans, D. H.; Glass, R. S.; Lichtenberger, D. L. *Organometallics* , ACS ASAP.
- (68) Durgaprasad, G.; Bolligarla, R.; Das, S. K. *J. Organomet. Chem.* **2011**, *696*, 3097.
- (69) Gao, S.; Fan, J.; Sun, S.; Song, F.; Peng, X.; Duan, Q.; Jiang, D.; Liang, Q. *Dalton Trans.* **2012**, *41*, 12064.

- (70) Petro, B. J.; Vannucci, A. K.; Lockett, L. T.; Mebi, C.; Kottani, R.; Gruhn, N. E.; Nichol, G. S.; Goodyer, P. A. J.; Evans, D. H.; Glass, R. S.; Lichtenberger, D. L. *J. Mol. Struct.* **2008**, *890*, 281.
- (71) Chiang, L. Y.; Shu, P.; Holt, D.; Cowan, D. *J. Org. Chem.* **1983**, *48*, 4713.
- (72) Tùng, Đ. T.; Tuân, Đ. T.; Rasool, N.; Villinger, A.; Reinke, H.; Fischer, C.; Langer, P. *Adv. Syn. Catal.* **2009**, *351*, 1595.
- (73) Manca, P.; Pilo, M. I.; Casu, G.; Gladiali, S.; Sanna, G.; Scanu, R.; Spano, N.; Zucca, A.; Zanardi, C.; Bagnis, D.; Valentini, L. *J. Polym. Sci., Part A: Polym. Chem.* **2011**, *49*, 3513.
- (74) Lagadec, A.; Dabard, R.; Misterkiewicz, B.; Le, R., Arlette; Patin, H. *J. Organomet. Chem.* **1987**, *326*, 381.
- (75) Anslyn, E. V.; Dougherty, D. A. In *Modern Physical Organic Chemistry*; University Science: Sausalito, CA, 2006; pp p147; Table 3.1.
- (76) Evans, D. H.; O'Connell, K. M.; Petersen, R. A.; Kelly, M. J. *J. Chem. Educ.* **1983**, *60*, 290.
- (77) Wright, R. J.; Zhang, W.; Yang, X.; Fasulo, M.; Tilley, T. D. *Dalton Trans.* **2012**, *41*, 73.
- (78) Felton, G. A. N.; Glass, R. S.; Lichtenberger, D. L.; Evans, D. H. *Inorg. Chem.* **2006**, *45*, 9181.
- (79) Kondo, T.; Okamura, M.; Uosaki, K. *J. Organomet. Chem.* **2001**, *637–639*, 841.
- (80) Hu, X.; Lin, Q.; Gao, J.; Wu, Y.; Zhang, Z. *Chem. Phys. Lett.* **2011**, *516*, 35.
- (81) Adams, C. J.; da Costa, R. C.; Edge, R.; Evans, D. H.; Hood, M. F. *J. Org. Chem.* **2010**, *75*, 1168.
- (82) Na, Y.; Wang, M.; Pan, J.; Zhang, P.; Åkermark, B.; Sun, L. *Inorg. Chem.* **2008**, *47*, 2805.